LARGE-EDDY SIMULATION USING A VORTEX-BASED SUBGRID STRESS MODEL

Thesis by

Ashish Misra

In Partial Fulfillment of the Requirements

for the Degree of

Doctor of Philosophy

California Institute of Technology

Pasadena, California

1998

(Submitted July 8, 1997)

Acknowledgements

I wish to gratefully acknowledge my advisor, Professor Dale Pullin. I am grateful for his supervision and honored to be his student. He painstakingly taught me the fundamentals of turbulence and ensured a steady pace of this thesis. The standards he sets for himself and his students are most impressive and noteworthy.

I acknowledge fruitful collaborations with Drs. Daniel Chan and Thomas Lund. Despite their busy schedule they unhesitatingly gave me their time and answered my seemingly endless questions. My trip to the Center for Turbulence Research, Stanford, was very productive and I thank Prof. Parviz Moin for giving me that opportunity. I also wish to acknowledge discussions with Prof. J. A. Domaradzki.

My friends in the computer lab - Mark Brady, Chris Eckett, Aure Prochazka, Shaun Shariff and Doug Shiels - kept me company during many dreary late nights through stimulating conversations. It has been a pleasure to associate with them.

I would like to thank my family for nurturing my academic interests from an early age. Special thanks are due to my sister, Anita Misra-Press, who was instrumental in bringing me to the US. My fiancée, Puja Kumar, was a constant source of motivation during the past year. I am grateful to her for being the truest friend. My room-mates Ranjan Mukhopadhyay and Rajit Manohar were a great help during the period of my illness.

Lastly, thanks are due to the Graduate Aeronautical Laboratories for rendering facilities and intellectual resources that I could count on. This work was supported in part by the National Science Foundation, NSF Grant CTS-9634222.

Abstract

A class of subgrid-stress (SGS) models for large-eddy simulation (LES) are presented based on the idea of structure-based subgrid-stress closure. The subgrid structure of the turbulence is assumed to consist of stretched vortices whose orientations are determined by the resolved velocity field. An equation which relates the subgrid stress to the structure orientation and the subgrid kinetic energy, together with an assumed Kolmogorov energy spectrum for the subgrid vortices, gives a closed coupling of the SGS model dynamics to the filtered Navier-Stokes equations for the resolved flow quantities. The subgrid energy is calculated directly by use of a local balance between the total dissipation and the sum of the resolved-scale dissipation and production by the resolved scales. Simple one- and two-vortex models are proposed and tested in which the subgrid vortex orientations are either fixed by the local resolved velocity gradients, or rotate in response to the evolution of the gradient field. These models are not of the eddy viscosity type. The choice of the energy spectrum introduces the Kolmogorov prefactor as a parameter. In the simplest case we make an *a priori* choice of the Kolmogorov prefactor which we refer to as the *fixed* $\mathcal{K}_0$ scheme. Alternatively, one can compute the Kolmogorov prefactor dynamically by enforcing continuity of the resolved energy spectrum with the subgrid spectrum. This introduces an additional equation for the Kolmogorov prefactor which is solved in conjunction with the equation relating the dissipation. This is referred to as the *coupled* $\mathcal{K}_0$ scheme. LES calculations with the present models are described for 32^3 decaying turbulence and also for forced 32^3 box turbulence at Taylor Reynolds numbers, R_λ, in the range $R_\lambda \simeq 30$ (fully resolved) to $R_\lambda = \infty$. The models give good agreement with experiment for decaying turbulence and produce negligible SGS dissipation for forced turbulence in the limit of fully resolved flow.

Using the *coupled* $\mathcal{K}_0$ scheme, we present LES results for a three-dimensional channel flow. The *coupled* $\mathcal{K}_0$ scheme is implemented in planes of constant height and the Kolmogorov prefactor is calculated as a function of the wall-normal direction by computing a two-dimensional energy spectrum. Results are presented for the alignment models in an

open channel of dimensions $4\pi \times 2\pi \times 2$ at a Reynolds number (based on the friction velocity and the channel half width), $R_\tau = 180$ and a grid resolution of $32 \times 32 \times 65$, where the last index refers to the wall-normal direction. Results compare favorably with direct numerical simulation (DNS).

Contents

List of Figures

Chapter 1

Introduction

Computing turbulent flows is one of the most challenging problems in computational fluid dynamics (CFD). Though CFD has enjoyed considerable progress in the last decade partially due to developments in computing hardware and software, the full range of scales for turbulence cannot be calculated directly for flows of engineering interest. Thus turbulence remains the main obstacle in the practical application of CFD. This chapter aims to introduce some of the existing methods used to compute turbulence and provides motivation for work presented in later chapters.

In a procedure devised by Reynolds (1895), we can write the instantaneous velocity as the sum of the mean, $\overline{U}_i$, and the fluctuation from the mean, u_i,

$$U_i(\mathbf{x},t) = \overline{U}_i(\mathbf{x},t) + u_i(\mathbf{x},t), \tag{1.1}$$

where the $\overline{\quad}$ denotes the time average defined as

$$\overline{U}_i(\mathbf{x},t) = \frac{1}{T}\int_{t-T}^{t} U_i(\mathbf{x},\tau)d\tau, \tag{1.2}$$

and T is an averaging time which must be long enough to smooth out the turbulent fluctuations but short enough not to average out any imposed time dependence. It follows from these definitions that the fluctuations themselves have zero mean. Averaging the incompressible Navier-Stokes equations according to (1.2), and using (1.1) and noting that $\overline{\overline{U}u} = \overline{U}\overline{u} = 0$, one obtains

$$\frac{\partial \overline{U}_i}{\partial x_i} = 0, \tag{1.3}$$

$$\frac{\partial \overline{U}_i}{\partial t} + \frac{\partial}{\partial x_j}\left(\overline{U}_i\overline{U}_j\right) = -\frac{\partial \overline{P}}{\partial x_i} - \frac{\partial}{\partial x_j}\overline{u_i u_j} + \nu\frac{\partial^2 \overline{U}_i}{\partial x_j \partial x_j}. \tag{1.4}$$

It is evident that the equation for the mean velocity is just the Navier-Stokes equation written in terms of the mean variables, but with the addition of the term involving $\overline{u_i u_j}$.

Thus the equation of the mean variables involves ten unknowns namely, $\overline{U}_i$, $\overline{P}$ and $\overline{u_i u_j}$. This is the classical closure problem in turbulence. Equation (1.4) is known as the *Reynolds-averaged Navier-Stokes equation* (RANS) and the term $\overline{u_i u_j}$ is known as the *Reynolds stress.*

1.1 Simulation techniques

The closure problem can be circumvented if we numerically solve the (unaveraged) Navier-Stokes equation. This approach is known as *direct numerical simulation* (DNS). If the mesh is fine enough to resolve the smallest scales of motion and the time stepping is fine enough to capture the fast time scales of the flow, then the only possible errors result from the discrete approximation of the equations. If L is the length scale of the computational domain and η, a measure of the small scales, then in order to resolve all the scales of motion one would need $N \sim L/\eta$ grid points in each direction. This ratio has been shown to be proportional to $Re^{3/4}$ (Landau and Lifshitz 1959). Thus the total number of grid points required in a DNS is proportional to $N^3 \sim Re^{9/4}$. Furthermore the number of time steps required to advance the computation for a given period, scales as $Re^{3/4}$. Given that the operation count in most CFD codes scale as $N^3 \log N$, the cost of doubling the Reynolds number would mean an increase in computational effort by a factor of 16. For this reason DNS has been restricted to simple geometries at low Reynolds numbers. Notwithstanding its limitations, DNS has effectively been applied to simple geometries such as flow past a flat plate, cylinder, channel flow, etc. and has been a useful tool towards understanding turbulence. Further discussions on this topic may be found in McComb (1990) and Rogallo and Moin (1984).

The other approach is to arrive at closure models for RANS. The effect of the turbulent fluctuations that appear in the Reynolds stresses must be modeled in order to close the system. Among the commonly used closure models for RANS are the mixing length models, the $k - \epsilon$ models and the algebraic Reynolds stress models (Spalding and Launder 1972). The most severe drawback of the RANS approach is its lack of generality. In most cases it involves setting many constants which have been derived for simple flow configurations. When these models are applied to flows which are very different than those used to calibrate these constants, *ad hoc* adjustments become necessary. This problem arises because the Reynolds stress contribution comes from a diversity of scales. While the smaller scales

may have some universal characteristics, the larger scales in most cases do not as they are strongly affected by the boundary conditions and the flow geometry. Notwithstanding its drawbacks, the RANS approach is easy to implement, considerably faster, and less memory intensive than DNS or LES.

Large-eddy simulation (LES) is an approach intermediate in complexity between the direct simulation of turbulence and the solution of Reynolds-averaged equations. The LES approach is to compute the detailed space and time dependence of the flow only at scales larger than some cutoff whilst modeling the effects on the retained scales of the transport of momentum and energy of the 'fine' scales below the cutoff. The approach is based on two related assumptions: first that the large (retained) scales are strongly coupled to the outer flow and the body geometry (boundary conditions) producing the turbulence, and second, that the 'fine' scales exhibit a quasi-universal character with only weak dependence on the large scales. The heart of LES is thus the construction of subgrid-stress (SGS) models which are based in some sense on a physically realistic description of the fine scales.

1.2 Filtered Navier-Stokes equations and subgrid stresses

The mathematical distinction between the 'fine' scales and the 'large' scales was formally introduced by Leonard (1974) as a convolution operation on the velocity field given by

$$\widetilde{U}_i(\mathbf{x},t) = \int G(\mathbf{x}-\mathbf{x}')U_i(\mathbf{x}',t)\mathbf{dx}', \tag{1.5}$$

where $G(\mathbf{x}-\mathbf{x}')$ is the kernel and the integral is over the entire domain. It may be shown that if G is solely a function of $\mathbf{x}-\mathbf{x}'$, then differentiation and the filtering operators commute (Leonard 1974). The most commonly used filter functions are the Gaussian and the top-hat filter in real space, and the sharp-cutoff filter function defined in wavenumber space.

Consider the large-eddy simulation of the Navier-Stokes equations on a grid with a typical cell size of Δx and time step Δt. Let $\widetilde{U}_i(\mathbf{x},t)$ represent the resolved (supergrid) velocity field and let $\widetilde{P}(\mathbf{x},t)$ be the resolved pressure field. The filtered LES equations for

an incompressible fluid are

$$\frac{\partial \widetilde{U}_i}{\partial x_i} = 0, \tag{1.6}$$

$$\frac{\partial \widetilde{U}_i}{\partial t} + \frac{\partial}{\partial x_j}\left(\widetilde{U}_i \widetilde{U}_j\right) = -\frac{\partial \widetilde{P}}{\partial x_i} - \frac{\partial T_{ij}}{\partial x_j} + \nu \frac{\partial^2 \widetilde{U}_i}{\partial x_j \partial x_j}, \tag{1.7}$$

where T_{ij} is the subgrid stress tensor defined as,

$$T_{ij} = \widetilde{U_i U_j} - \widetilde{U}_i \widetilde{U}_j. \tag{1.8}$$

Furthermore, if the subgrid velocity is decomposed as $U_i(\mathbf{x}, t) = \widetilde{U}_i(\mathbf{x}, t) + u_i(\mathbf{x}, t)$ where U_i is the full velocity field and u_i the subgrid field then the subgrid stress tensor may be broken into three parts,

$$T_{ij} = L_{ij} + C_{ij} + R_{ij} \tag{1.9}$$

where $L_{ij} = \widetilde{\widetilde{U}_i \widetilde{U}_j} - \widetilde{U}_i \widetilde{U}_j$ are the Leonard stresses, $C_{ij} = \widetilde{u_i \widetilde{U}_j} + \widetilde{u_j \widetilde{U}_i}$ are the cross-terms and $R_{ij} = \widetilde{u_i u_j}$ are the SGS Reynolds stresses. The Leonard stresses represent interactions between resolved scales that result in subgrid scale contributions. They can be computed explicitly given the choice of the filter. For a sharp-cutoff filter they are the aliasing errors. The cross-terms represent interactions between the resolved and the unresolved scales whereas the SGS Reynolds stresses represent the contribution from the unresolved scales.

A further complication concerns the question of filtering in time. At large Reynolds numbers, equations (1.6-1.7) appear to have little physical meaning on time-scales of the order of the Kolmogorov time-scale, $(\nu/\epsilon)^{1/2}$, and shorter. In fact, time-wise integration of (1.6-1.7) is usually done with time-step $\Delta t_L >> (\nu/\epsilon)^{1/2}$ which implies a filter. It would therefore seem prudent to generalize (1.5) to a space-time filter, with no change in the formalism. This issue does not seem to have been addressed in the literature but may be relevant to proper comparison of LES and filtered DNS.

1.3 Review of some SGS models

Most popular SGS models use Smagorinsky's realization of the eddy-viscosity model. The subgrid stresses are written as (Smagorinsky 1963)

$$\tau_{ij} - \frac{1}{3}\,\delta_{ij}\tau_{kk} = -2\,(C\,\Delta)^2|\widetilde{S}|\widetilde{S}_{ij}, \tag{1.10}$$

where $\widetilde{S}_{ij} = \left(\partial\widetilde{U}_i/\partial x_j + \partial\widetilde{U}_j/\partial x_i\right)/2$ is the resolved rate-of-strain tensor, $|\widetilde{S}|^2 = 2\widetilde{S}_{ij}\widetilde{S}_{ij}$, and C is a dimensionless number called the Smagorinsky coefficient. Δ is some characteristic length scale, i.e. the scale below which (1.5) represents the effect of the averaged motion of the neglected scales. Values of C in the range $0.1 - 0.2$ have been used. A difficulty with assuming C to be constant is that the eddy viscosity overwhelms the molecular viscosity in regions of laminar flow. The Smagorinsky based models have proved useful but do have some drawbacks, one of which is that, owing to their phenomenological origin, the models provide no direct estimate of subgrid contributions to turbulent transport.

In the "dynamic model" (Germano et al. 1991; Ghosal et al. 1995), this problem is handled by use of a procedure based on evaluating the Leonard stresses at various filter scales, together with certain kinematical identities to develop techniques for computing $C(\mathbf{x}, t)$ as the LES computation proceeds. Some other eddy viscosity type models that have met with mixed success are the spectral-eddy viscosity model (Kraichnan 1976) and the structure function model (Metais and Lesieur 1992). A few alternatives to eddy viscosity type models have been proposed, including the scale-similarity model (Bardina et al. 1980), a model based on estimation of part of the unresolved velocity field and a tensor-diffusivity model which utilizes a direct evaluation of the non-linear terms by a series expansion and estimating the low order term (Leonard 1997). These and other developments in LES modeling are reviewed by Reynolds (1989) and Lesieur (1996).

In a recent attempt to model the SGS stresses, Domaradzki and Saiki (1996) propose a velocity estimation method for the unfiltered velocity field. The subgrid stresses can then be calculated using (1.8). An estimate for the unfiltered velocity field is obtained by expanding the resolved large scale velocity field to subgrid scales two times smaller than the grid scale. The rationale for such an extrapolation comes from their study which shows that approximately 75% of the SGS energy transfer is from the range of resolved scales $0.5k_c < k < k_c$, where k_c is the cutoff wavenumber. DNS data also reveals that almost the

entire SGS energy transfer is exclusively by interactions of the resolved scales with a limited range of subgrid scales with wavenumbers $k_c < k < 2k_c$.

In this thesis we discuss a structural SGS model put forward by Pullin and Saffman (1994). The model stems from the physics of the 'fine' scales of turbulence and is not of the eddy viscosity type. In Chapter 2 we discuss and further develop the stretched vortex models. The application of these models in homogeneous turbulence is presented in Chapter 3. We discuss the case of the Taylor-Green vortex followed by a detailed investigation of decaying and forced isotropic turbulence. The performance of these models in a three-dimensional channel flow are presented in Chapter 4. Conclusions and future work are discussed in Chapter 5.

Chapter 2

Stretched vortex subgrid models

We propose a structural model of the subgrid vorticity based on a stretched-vortex representation of the subgrid scales. Structure-based models designed for turbulence computation were discussed by Reynolds (1992) and specific models have been proposed by Pullin and Saffman (1994), henceforth PS, aimed at SGS modeling for LES, and by Reynolds and Kassinos (1995) in the context of one-point closure for RANS. The general approach may be characterized as *structure-based subgrid stress closure*. In this chapter we implement and further develop the stretched-vortex subgrid model of PS. Some of this work is reported by Misra and Pullin (1997).

2.1 Basic model structure

The subgrid vorticity is assumed to consist of a superposition of vorticity fields or 'structures', each with the property that the vorticity is unidirectional, with its magnitude having no explicit dependence on the coordinate parallel to the vorticity. Some support for this structure is provided by the observed tendency for alignment between the vorticity vector and the eigenvector corresponding to the algebraically intermediate principal rate-of-strain, in several numerical simulations (Ashurst et al. 1987; Vincent and Meneguzzi 1991). This suggests a small-scale structure which is nearly "two-dimensional," stretched by strain which is weaker than the small-scale vorticity. Special cases are the Burgers-Townsend vortex (Townsend 1951) and the Lundgren stretched-spiral vortex (Lundgren 1982) both of which have been applied to calculation of fine-scale turbulence properties (Pullin and Saffman 1993; Pullin et al. 1994). The success of the stretched-vortex models of the fine scales, while mixed, does suggest that they may form the basis of a viable SGS model for LES. In what follows we give a description of the subgrid vortex orientation and an expression for the subgrid stresses. When combined with schemes for relating the vortex orientation and the subgrid turbulent energy to the resolved scales, a closed system of LES

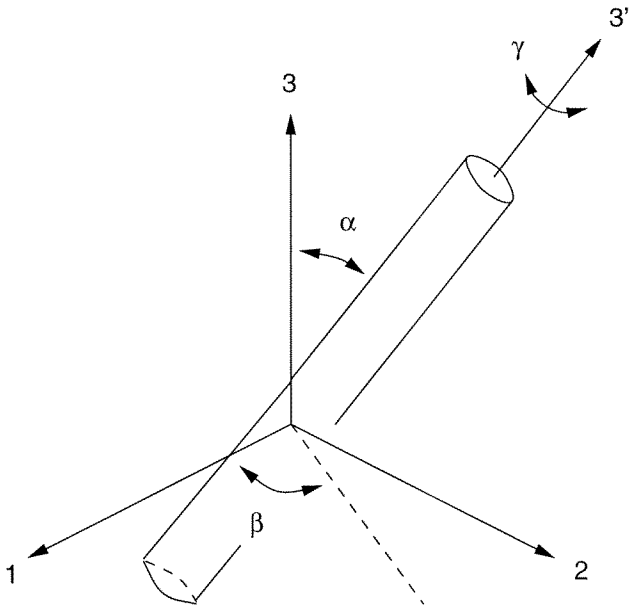

Figure 2.1: Orientation of the vortex axes with respect to the laboratory-fixed axes.

equations results.

2.1.1 Vortex structure

Since the main problem of SGS modeling for LES is to represent the averaged effect of the small scales on the dynamics of the resolved scales, there is less need for a detailed subgrid vorticity distribution than is required by calculation of the fine scale properties themselves. Here we discuss a simple model of a typical subgrid structure put forth by PS. The homogenous turbulence is assumed to consist of a superposition of velocity fields from an ensemble of straight vortex structures. The orientation of a particular structure is shown with respect to the laboratory axes in Figure 2.1. We take axes (r_1, r_2, r_3) with corresponding unit vectors $(\mathbf{e_1}, \mathbf{e_2}, \mathbf{e_3})$ fixed in space and define the unit vectors of a particular structure with $\mathbf{e_3'}$ parallel to the vorticity in the structure. It is assumed by PS that the vorticity within each structure is always parallel to the vortex axis, i.e.

$$\omega = \omega(r_1', r_2', t)\mathbf{e_3'}, \tag{2.1}$$

where (r_1', r_2', r_3') are the coordinates in the vortex-fixed axes with (r_1', r_2') lying in a plane normal to the vortex axis. PS refer to this as *cylindrically unidirectional.* An essential assumption in the PS model is that the structures maintain their unidirectionality during

any interactions between the structures and the large scales. The motions inside the vortices satisfy the Navier-Stokes equations and we further note that the vortex/Navier-Stokes dynamics enters in an implicit way to be discussed later in this section (see also Appendix B).

Let E_{ij} denote the rotation tensor describing the transformation of coordinates from the laboratory-fixed axes, (r_1, r_2, r_3), to the vortex-fixed axes, $(r_1^{'}, r_2^{'}, r_3^{'})$. This rotation may be described in terms of the three Euler angles - α, the colatitude angle (the angle between the r_3 axis and the $r_3^{'}$ axis), β is the longitude angle and γ the spin angle about the $r_3^{'}$ axis (see, e.g., Jeffreys and Jeffreys (1950)). Thus E_{ij} may be written as,

$$\mathsf{E} = \begin{pmatrix} \cos\alpha\cos\beta\cos\gamma - \sin\beta\sin\gamma & \cos\alpha\sin\beta\cos\gamma + \cos\beta\sin\gamma & -\sin\alpha\cos\gamma \\ -\cos\alpha\cos\beta\sin\gamma - \sin\beta\cos\gamma & -\cos\alpha\sin\beta\sin\gamma + \cos\beta\cos\gamma & \sin\alpha\sin\gamma \\ \sin\alpha\cos\beta & \sin\alpha\sin\beta & \cos\alpha \end{pmatrix}. \tag{2.2}$$

2.1.2 Subgrid stresses

In the $(r_1^{'}, r_2^{'}, r_3^{'})$ axes, PS show that the SGS stresses, when averaged over the structure cross-section, may be given by,

$$\overline{u_i^{'} u_j^{'}} = \overline{u_m^{'\,2}}\, \mathsf{Z}_{ij}, \tag{2.3}$$

where Z_{ij} is a diagonal tensor with diagonal elements $\left(\frac{1}{2}, \frac{1}{2}, 0\right)$. In equation (2.3), the $\overline{\text{“ ”}}$ is defined to be an average over the cross section of the vortex, followed by an average over all possible spin orientations of the vortex γ, where γ is assumed to be uniformly distributed in $0 \leq \gamma \leq 2\pi$. $\overline{u_m^{'\,2}}$, is thus the mean square velocity averaged across the vortex cross section and orientation. PS give several formal and heuristic derivations of (2.3). The simplest way to understand (2.3) is to realize that owing to the assumed distribution given by (2.1) the velocity associated with the vortex motion must lie in the $(r_1^{'}, r_2^{'})$ plane, so that when the average over $(r_1^{'}, r_2^{'})$ plane and over γ is taken, the off-diagonal components will vanish and the turbulent energy will be distributed equally in the $r_1^{'}$ and the $r_2^{'}$ directions. Upon transforming back to the laboratory-fixed axes we obtain,

$$\tau_{ij} = \overline{u_m^2}\quad \mathsf{E}_{pi}\mathsf{Z}_{pq}\mathsf{E}_{qj}, \tag{2.4}$$

where,

$$\mathsf{E}^{\mathsf{T}} \cdot \mathsf{Z} \cdot \mathsf{E} = \begin{pmatrix} \frac{1}{2}(1-\sin^2\alpha\cos^2\beta) & -\frac{1}{4}\sin^2\alpha\sin 2\beta & -\frac{1}{4}\sin 2\alpha\cos\beta \\ -\frac{1}{4}\sin^2\alpha\sin 2\beta & \frac{1}{2}(1-\sin^2\alpha\sin^2\beta) & -\frac{1}{4}\sin 2\alpha\sin\beta \\ -\frac{1}{4}\sin 2\alpha\cos\beta & -\frac{1}{4}\sin 2\alpha\sin\beta & \frac{1}{2}(1-\cos^2\alpha) \end{pmatrix}. \tag{2.5}$$

We further note that $\mathsf{E}^{\mathsf{T}} \cdot \mathsf{Z} \cdot \mathsf{E}$ is independent of γ.

We now introduce the pdf $P(\alpha, \beta)$ of the vortex Euler angles, such that $P \sin\alpha\, d\alpha\, d\beta/4\pi$ is the probability that $(\mathbf{e}_1', \mathbf{e}_2', \mathbf{e}_3')$ lie in the range α to $\alpha + d\alpha$ and β to $\beta + d\beta$. In general $P(\alpha, \beta)$ may be expected to be determined by interaction between the small and large-scale motions. Our models for this will be discussed later. The expectation over any function $f(\mathsf{E}_{ij})$ averaged over the orientation may be defined as,

$$\langle f(\mathsf{E}_{ij})\rangle = \frac{1}{4\pi}\int_0^{\pi}\int_0^{2\pi} f(\mathsf{E}_{ij}) P(\alpha,\beta)\sin\alpha\, d\alpha\, d\beta. \tag{2.6}$$

Applying (2.6) to (2.4) then yields,

$$\tau_{ij} = \overline{u_m^2}\quad \langle \mathsf{E}_{pi}\mathsf{Z}_{pq}\mathsf{E}_{qj}\rangle, \tag{2.7}$$

where it is assumed that $\overline{u_m^2}$ is independent of (α, β).

Using the standard result from homogeneous turbulence (Batchelor 1953), the subgrid energy may be written as,

$$\overline{u_m^2} = 2K \tag{2.8}$$

$$K \equiv \int_{k_c}^{\infty} E(k)\, dk, \tag{2.9}$$

where, $E(k)$ is the subgrid energy spectrum and k_c is the cutoff wavenumber. We thus obtain, the SGS stresses as,

$$\tau_{ij} = 2K\quad \langle \mathsf{E}_{pi}\mathsf{Z}_{pq}\mathsf{E}_{qj}\rangle. \tag{2.10}$$

The internal and unknown vorticity distribution need not be axisymmetric. Equation (2.10) holds for an arbitrary internal vorticity distribution in an individual structure following averaging over spin angles γ about the vortex axis, when γ is assumed uniformly distributed in $0 \leq \gamma \leq 2\pi$. Equation (2.10) is nevertheless operationally equivalent to an

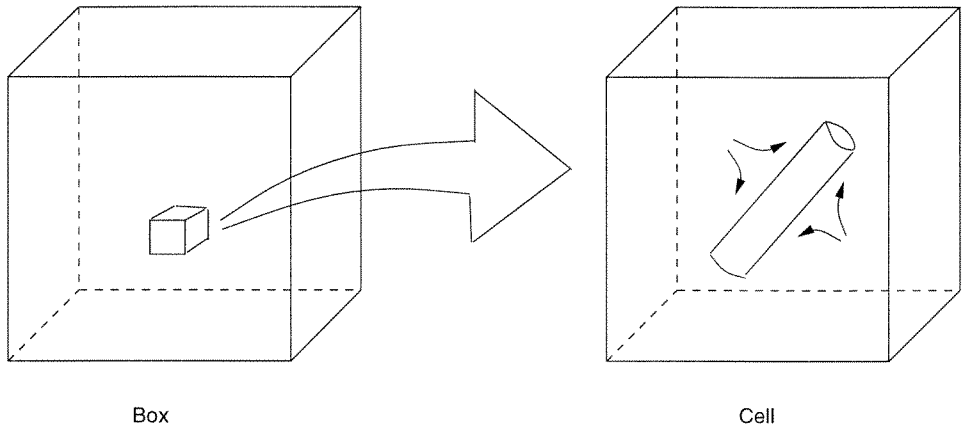

Figure 2.2: A typical cell representing the fine scales, showing a single vortex embedded in a strain field $\partial\widetilde{U}_i/\partial x_j$, provided by the large scales.

axisymmetric subgrid vortex. This may be justified physically by arguing that at sufficiently large Reynolds number and for sufficiently small k_c, the subgrid vortex dynamics may be assumed to be evolving on a time scale which is fast compared to Δt_L the integration time-step for (1-4). In Δt_L either some degree of subgrid dynamic axisymmetrization can be expected, or, alternatively owing to its self-induced motion about its axis, some azimuthal averaging, equivalent to a sampling of the space of state spin angles, will occur, thus giving a tendency to equipartition. We remark that (2.10) has a similar structure to the "dimensionality tensor" of Reynolds (1992).

The stretched vortex model of the subgrid vorticity is very simple. It is effectively a locally two-dimensional model of the subgrid motion. Possible axial motions inside the vortex are neglected and so are reconnections of the subgrid vorticity with neighboring structures. The essential idea of the model is illustrated in Figure 2.2, where the vortex is embedded in a strain field which is provided locally by the resolved velocity gradient tensor $\partial\widetilde{U}_i/\partial x_j$. The main physical idea is that the vortex gets stretched/compressed and rotated by $\partial\widetilde{U}_i/\partial x_j$. When stretched, the component of $\partial\widetilde{U}_i/\partial x_j$ aligned with the vortex axis will be much weaker than the internal strain field of the small-scale two-dimensional motion inside the vortex. This will have the effect that the vorticity will align with the intermediate eigenvector of the total local strain field. This was referred to earlier as the characteristic of the fine scales observed in DNS.

2.2 Vortex orientation models

Calculation of τ_{ij} from (2.10) requires both K and the distribution of structure orientations. PS proposed that the subgrid vortex structures are convected and rotated by the resolved field. The equation describing the evolution of $P(\alpha, \beta)$ is then

$$\frac{\partial P}{\partial t} + \widetilde{U}_j \frac{\partial P}{\partial x_j} + \frac{1}{\sin\alpha}\frac{\partial}{\partial \alpha}\left(\widetilde{U}_\alpha \sin\alpha\, P\right) + \frac{1}{\sin\alpha}\frac{\partial}{\partial \beta}\left(\widetilde{U}_\beta\, P\right) = 0, \tag{2.11}$$

where $\widetilde{U}_\alpha, \widetilde{U}_\beta$ are the projections of the resolved field $r_j\, \partial \widetilde{U}_i / \partial x_j$ onto the unit sphere. The third and fourth terms of (2.11) give the contribution to the rate of change of P from rotation by $\partial \widetilde{U}_i / \partial x_j$. The use of (2.11) is justified by heuristic appeal to the ideas of rapid distortion theory in the context of the present structural model. In the cells, individual vortices feel the local strain provided by the resolved field and rotate in response. In the PS model, the subgrid energy was determined by assuming that $E(k)$ had a locally Kolmogorov form. The local dissipation ϵ was calculated by relating it to the sum of the local production plus the local dissipation in the resolved field. This model, with appropriate boundary conditions for P gives closure. It is not of the eddy-viscosity type.

We tried to solve (2.11) using an ellipsoidal model for $P(\alpha, \beta)$ (See appendix A). This was unsuccessful as it was found that the ellipsoid rapidly evolved into a "cigar" irrespective of its initial conditions. This is consistent with the analysis of Cocke (1969) and later Orszag (1970), who showed that for homogeneous isotropic turbulence the length of a material line always increases on the average with time. This led us to the natural choice of delta-function pdf models. Presently we describe an approach based on modeling $P(\alpha, \beta)$ by product delta functions or a linear combination of products of delta functions. Typically we have

$$P(\alpha, \beta) = \frac{4\pi}{\sin\alpha}\, \delta(\alpha - \theta)\, \delta(\beta - \phi) \equiv \wp\left(\mathbf{e} \mid \mathbf{e}^v\right), \tag{2.12}$$

where $\theta(\mathbf{x}, t)$, $\phi(\mathbf{x}, t)$ is the specific orientation, and where the unit vectors $\mathbf{e}$ and $\mathbf{e}^v$ are defined respectively by

$$e_1 = \sin\alpha\cos\beta, \qquad e_2 = \sin\alpha\sin\beta, \qquad e_3 = \cos\alpha, \tag{2.13}$$

$$e_1^v = \sin\theta\cos\phi, \qquad e_2^v = \sin\theta\sin\phi, \qquad e_3^v = \cos\theta. \tag{2.14}$$

We have introduced the notation $\wp(\mathbf{e} \mid \mathbf{e}^v)$ for convenience. While this almost certainly oversimplifies the subgrid vortex dynamics, the spirit of LES is to obtain the averaged effect of subgrid motions on resolved scales, and it is hoped that (2.12) will suffice for this purpose.

It then follows from (2.5) and (2.12) that equation (2.10) can be written as

$$\tau_{ij} = (\delta_{ij} - e_i^v\, e_j^v) \int_{k_c}^{\infty} E(k)\, dk. \tag{2.15}$$

We now describe some specific orientation models used presently. The first two align the vortices with directions defined by the local resolved strain rates. We refer to these as *local alignment models.* They are simple and easy to implement. The third model attempts to couple the vortex orientation to the evolution of the resolved rate-of-strain tensor.

2.2.1 Model 1a: Alignment with $\tilde{\mathbf{e}}_3$ and $\tilde{\mathbf{e}}_2$

This model, proposed by PS, is based on the idea that the subgrid structures respond on a fast time scale to the supergrid strain. Let the eigenvectors of $\widetilde{S}_{ij}$, be $\tilde{\mathbf{e}}_1$, $\tilde{\mathbf{e}}_2$ and $\tilde{\mathbf{e}}_3$, corresponding to eigenvalues $\lambda_1 < \lambda_2 < \lambda_3$, such that $\lambda_1 + \lambda_2 + \lambda_3 = 0$. It is assumed that a fraction of the local subgrid structures tend to become aligned with $\tilde{\mathbf{e}}_3$ and the remainder align with the intermediate eigenvector $\tilde{\mathbf{e}}_2$. The orientation pdf is a two-vortex model given by

$$P(\mathbf{e}) = \lambda\, \wp(\mathbf{e} \mid \tilde{\mathbf{e}}_3) + (1 - \lambda)\, \wp(\mathbf{e} \mid \tilde{\mathbf{e}}_2)\,, \tag{2.16}$$

where,

$$\lambda = \frac{\lambda_3}{|\lambda_2| + \lambda_3}. \tag{2.17}$$

With equipartition of subgrid energy among the vortices, τ_{ij} is given by,

$$\tau_{ij} = [\lambda(\delta_{ij} - \tilde{e}_{3i}\tilde{e}_{3j}) + (1 - \lambda)(\delta_{ij} - \tilde{e}_{2i}\tilde{e}_{2j})] \int_{k_c}^{\infty} E(k) dk. \tag{2.18}$$

2.2.2 Model 1b: Alignment with $\tilde{\mathbf{e}}_3$ and the resolved vorticity vector, $\tilde{\omega}$

Model 1a will be later shown to contain no backscatter i.e., the subgrid structures are subject only to stretching. In order to allow for backscatter we propose the model

$$P(\mathbf{e}) = \mu\, \wp\left(\mathbf{e} \mid \tilde{\mathbf{e}}_3\right) + (1-\mu)\, \wp\left(\mathbf{e} \mid \mathbf{e}^{\omega}\right), \tag{2.19}$$

$$\tau_{ij} = \left[\mu(\delta_{ij} - \tilde{e}_{3i}\tilde{e}_{3j}) + (1-\mu)(\delta_{ij} - e_i^{\omega} e_j^{\omega})\right] \int_{k_c}^{\infty} E(k)dk, \tag{2.20}$$

where $(1-\mu)$ is the fraction of structures aligned with the resolved vorticity, with direction $e_j^{\omega} = \tilde{\omega}_j/|\tilde{\omega}|$, where $\tilde{\omega}$ is the resolved vorticity. This model is arbitrary but can be shown to include backscatter. As partial justification we note that we should expect complete alignment with $\tilde{\omega}$ in the DNS limit. We have performed calculations with $\mu = 0, 0.5, 1.0$.

2.2.3 Model 2: Rotation by $\widetilde{A}_{ij}$

The *local alignment models* make no use of (2.11). A realizable model intermediate in complexity between (2.11) and Models 1a-b can be obtained by substituting (2.12) into (2.11) and using (2.14) to yield

$$\frac{\partial e_i^v}{\partial t} = e_j^v\, \tilde{A}_{ij} - e_i^v\, e_k^v\, e_j^v\, \tilde{A}_{kj}, \tag{2.21}$$

where

$$\tilde{A}_{ij} \equiv \frac{\partial \widetilde{U}_i}{\partial x_j}, \tag{2.22}$$

is the resolved velocity-gradient tensor. In practice, owing to the need for de-aliasing arising in the implementation of spectral methods, it is more convenient to work with the equation for a vector defined by $\ell_i = Q(\mathbf{x}, t)\, e_i^v$. If $Q(\mathbf{x}, t)$ is chosen such that $\vec{\ell}$ is a solenoidal field equation (2.21) can be written as

$$\frac{\partial \ell_i}{\partial t} - \frac{\partial}{\partial x_j}\left(\ell_j \widetilde{U}_i\right) = 0. \tag{2.23}$$

It is straightforward to show that the axis of a straight compact vortex, with an arbitrary internal vorticity distribution, when embedded in a time-dependent outer strain field, will rotate according to equation (2.21). We remark that in obtaining (2.23) we have omitted

convection of the subgrid vortices by the resolved field. This is done since no coupling of vortices in neighboring cells is assumed. Thus two vortices originating at different locations can be brought arbitrarily close together with differing orientations. Some discussion on an equation of the type (2.23) may be found in Bayly (1992). An alternative is to introduce a model damping mechanism, which we wish to avoid. In Appendix B an alternative derivation of (2.21) is presented.

2.3 Subgrid energy and dissipation

Closure of all the aforementioned models requires knowledge of the subgrid energy K. Our present method of evaluating K, invokes a local balance between the total dissipation and the sum of the resolved-scale dissipation and the production of turbulent kinetic energy by the interaction between the resolved rate-of-strain tensor and the subgrid stresses. An alternative approach based on $K-\epsilon$-type equations for the subgrid vortices is discussed in Chapter **V** but is not implemented in this study.

We develop the local balance arguments for a generic single-vortex model with SGS stresses given by (2.15); they can be *mutatis mutandis* carried out for the alignment Model 1a and Model 1b and the rotation model respectively. It is assumed that the difference between the total local dissipation ϵ, and the resolved-scale viscous dissipation is in balance with the local supergrid energy production, ε_{sgs}, so that

$$\epsilon = 2\nu\widetilde{S}_{ij}\widetilde{S}_{ij} + \varepsilon_{sgs}, \qquad \varepsilon_{sgs} \equiv -\widetilde{S}_{ij}\tau_{ij} = -K\,\widetilde{S}_{ij}(\delta_{ij} - e_i^v\, e_j^v). \tag{2.24}$$

Closure is obtained by assuming a Kolmogorov form of $E(k)$ with a viscous cutoff

$$\begin{aligned} E(k) &= \mathcal{K}_0\,\epsilon^{2/3}\,k^{-5/3}, \qquad && k_c < k < \eta^{-1} \\ &= 0, && k > \eta^{-1}, \end{aligned} \tag{2.25}$$

where $\mathcal{K}_0$ is the Kolmogorov prefactor and $\eta = (\nu^3/\epsilon)^{\frac{1}{4}}$ is the local Kolmogorov length. We remark that for stretched vortex models of the fine scales $E(k)$ depends only on the internal structure of the vorticity and is independent of $P(\mathbf{e})$ (Pullin and Saffman 1994; Lundgren 1982); there is no assumption of isotropy and therefore no inconsistency in combining a Kolmogorov spectrum with local anisotropy. Alternatives to the sharp dissipation cutoff

of (2.25) would be to assume that each subgrid vortex is of the Lundgren spiral vortex form, and to replace (2.25) with the Lundgren spectrum, or to use an exponential cutoff near $k\eta = 1$ as suggested by DNS (Kida and Murakami 1987) and experiment (Saddoughi and Veeravalli 1994). The sharp cutoff is chosen presently for simplicity; at large Reynolds numbers the energy integral converges absolutely when (2.25) is used and $\nu \to 0$. At low Reynolds number, the model subgrid stresses are subdominant to the resolved viscous stresses (see PS, Appendix B). The actual form of the dissipation range $E(k)$ would be important if one were trying to predict the distribution of the dissipation across the subgrid scales, but the spirit of LES is to get the averaged effects, without having to compute all the subgrid details, and we expect a simple model to be sufficient for this purpose. We remark that (2.25) can be viewed as introducing a cutoff parameter $k\eta = J$, where we have chosen $J = 1$. Finally, it might be objected that (2.25) is inconsistent with the effective axisymmetric vortex structure. We again emphasize the PS kinematic derivation of (2.10) is for an arbitrary internal vorticity distribution when the average over uniformly distributed spin angles is allowed.

Using (2.25) in (2.15) the subgrid stresses may be expressed as,

$$\begin{aligned} \tau_{ij} &= \frac{3\,\mathcal{K}_0}{2\,k_c^{2/3}}\,\epsilon^{2/3}\left(1 - (k_c\eta)^{2/3}\right)(\delta_{ij} - e_i^v\,e_j^v), && k_c\eta < 1 \\ &= 0, && k_c\eta > 1. \end{aligned} \tag{2.26}$$

When equation (2.26) is substituted in equation (2.24) one obtains,

$$\begin{aligned} \epsilon &= 2\nu\widetilde{S}_{ij}\widetilde{S}_{ij} - \frac{3\,\mathcal{K}_0}{2\,k_c^{2/3}}\,\epsilon^{2/3}\left(1 - (k_c\eta)^{2/3}\right)\widetilde{S}_{ij}(\delta_{ij} - e_i^v\,e_j^v), && k_c\eta < 1 \\ &= 2\nu\widetilde{S}_{ij}\widetilde{S}_{ij}, && k_c\eta > 1, \end{aligned} \tag{2.27}$$

which, upon using the transformation

$$X = k_c\eta = k_c\left(\frac{\nu^3}{\epsilon}\right)^{1/4}, \tag{2.28}$$

gives

$$1 - \widehat{S}_1 X^4 + 3\mathcal{K}_0\widehat{S}_2 X^{4/3}(1 - X^{2/3}) = 0, \qquad X < 1 \tag{2.29}$$

$$1 - \widehat{S}_1 X^4 = 0, \qquad X > 1,$$

where,

$$\widehat{S}_1 = \frac{2\widetilde{S}_{ij}\widetilde{S}_{ij}}{k_c^4 \nu^2}, \tag{2.30}$$

$$\widehat{S}_2 = \widetilde{S}_{ij} \frac{(\delta_{ij} - e_i^v\, e_j^v)}{2\, k_c^2 \nu}. \tag{2.31}$$

It can be shown that for $\widehat{S}_1 > 0$ (2.29) always has a positive real root. It will later be demonstrated that (2.29) can have multiple solutions for X in certain regions of $\widehat{S}_1 - \widehat{S}_2$ space, but these will be seen to be well removed from realizable values of $\widehat{S}_1, \widehat{S}_2$. The required solution is defined as that on a continuous branch from the positive solution corresponding to $\widehat{S}_2 = 0$. When $\widehat{S}_1 < 1$ this can be shown to satisfy $X > 1$, which from (2.26) gives zero subgrid stresses, while for $\widehat{S}_1 > 1$ this branch gives $X < 1$ always. Hence in practice the first of (2.29) is solved only when $\widehat{S}_1 > 1$; otherwise the SGS model turns off, or equivalently, we set $X = 1$. This corresponds to locally fully resolved flow.

For the defined branch, dominant balance arguments can be used to show that in the limit of $\nu \to 0$

$$\epsilon = \frac{27\, \mathcal{K}_0^3}{8\, k_c^2} \left(-\widetilde{S}_{ij}(\delta_{ij} - e_i^v\, e_j^v) \right)^3, \qquad \hat{S}_2 < 0 \tag{2.32}$$

$$= 0, \qquad \hat{S}_2 > 0. \tag{2.33}$$

Equation (2.29) is our basic result for calculating the dissipation, from which the subgrid stresses follow from (2.26). Presently we use (2.29) in two different implementations. In the first, $\mathcal{K}_0$ is specified as a parameter and is held fixed for the simulation. This is the *fixed* $\mathcal{K}_0$ scheme. In the second implementation, $\mathcal{K}_0$ is calculated dynamically as follows; label the points in physical space at which the resolved field is calculated by index $m = 1, \ldots M$, where, for example, $M = N^3$ for an N^3 spectral method. Next, write (2.29) at each point of the resolved flow in physical space as

$$H\left[\widehat{S}_{1,m} - 1\right] \left(1 - \widehat{S}_{1,m}\, X_m^4 + 3\mathcal{K}_0 \widehat{S}_{2,m}\, X_m^{4/3}(1 - X_m^{2/3})\right) + H\left[1 - \widehat{S}_{1,m}\right](1 - X_m) = 0, \qquad m = 1, \ldots M, \tag{2.34}$$

where $H[\ldots]$ denotes the Heaviside function, $X_m = k_c(\nu^3/\epsilon_m)^{1/4}$, ϵ_m being the local dissipation at point m, and $\widehat{S}_{1,m}$, $\widehat{S}_{2,m}$ are (2.30) and (2.31) evaluated at point m.

Now let $\tilde{E}(\tilde{k})$ be the energy spectrum of the resolved field at some specified wavenumber $k = \tilde{k}$, $\tilde{k} < k_c$. Assume that $\tilde{E}(\tilde{k})$ conforms to (2.25)

$$\tilde{E}(\tilde{k}) = \mathcal{K}_0 \langle\epsilon\rangle^{2/3} \tilde{k}^{-5/3}, \tag{2.35}$$

where $\langle\epsilon\rangle$ is the instantaneous volume-averaged dissipation, which can be expressed as

$$\langle\epsilon\rangle = \frac{1}{M}\sum_{m=1}^{M} H\left[\widehat{S}_{1,m} - 1\right]\frac{\nu^3 k_c^4}{X_m^4} + H\left[1 - \widehat{S}_{1,m}\right] 2\nu\widetilde{S}_{ij}\widetilde{S}_{ij}. \tag{2.36}$$

Equation (2.35) forces continuity of the resolved and subgrid energy spectra at $k = \tilde{k}$, which in practice is chosen near to, but somewhat less than k_c. Eliminating $\langle\epsilon\rangle$ from (2.35) and (2.36) gives

$$\frac{\hat{F}}{\mathcal{K}_0^{3/2}} - \frac{1}{M}\sum_{m=1}^{M} H\left[\widehat{S}_{1,m} - 1\right]\frac{1}{X_m^4} + H\left[1 - \widehat{S}_{1,m}\right]\hat{S}_{1,m} = 0, \tag{2.37}$$

where,

$$\hat{F} = \frac{\tilde{E}^{3/2}\tilde{k}^{5/2}}{\nu^3 k_c^4}. \tag{2.38}$$

When M, k_c, $\tilde{k}$, $\tilde{E}$, ν and $\widehat{S}_{1,m}$, $\widehat{S}_{2,m}$ are given, (2.34) and (2.37) are $M+1$ nonlinear equations for X_m $(m = 1, \ldots M)$ and $\mathcal{K}_0$. Once the X_m are known, the ϵ_m can be calculated and the subgrid stresses follow from (2.26) applied at each point. We refer to this as the *coupled* $\mathcal{K}_0$ scheme. The methods by which the *fixed* $\mathcal{K}_0$ and the *coupled* $\mathcal{K}_0$ schemes are incorporated into an LES code are described in the following chapters.

Chapter 3

Homogeneous flows - turbulence in a periodic box

We apply the models developed in the previous chapter to homogeneous flows. In §3.1 we illustrate the numerical procedure incorporated in these simulations. We then present results in §3.2 for the Taylor-Green problem. In §3.3 we discuss the important case of isotropic turbulence; §3.3.1 deals with decaying turbulence, such flows are discussed extensively in Batchelor (1953) and can be generated behind a grid in a laboratory wind tunnel. We compare our results for this case with the experiments of Comte-Bellot and Corrsin (1971). In §3.3.2 we present results for forced isotropic turbulence for all models. Some comparison with DNS is also made.

The results presented in the following sections are obtained using the *coupled* $\mathcal{K}_0$ scheme. The *fixed* $\mathcal{K}_0$ scheme gives almost identical results with the appropriate value of $\mathcal{K}_0$ chosen. The *fixed* $\mathcal{K}_0$ scheme will be referred to by F-$\mathcal{K}_0$[...] and the *coupled* $\mathcal{K}_0$ scheme by C-$\mathcal{K}_0$[...]. The bracketed information indicates the model number, i.e., 1a, 1b or 2. For example F-$\mathcal{K}_0$[1a] would refer to Model 1a with $\mathcal{K}_0$ held fixed while C-$\mathcal{K}_0$[1b; 0.5] would refer to Model 1b with $\mu = 0.5$ using the *coupled* $\mathcal{K}_0$ scheme.

3.1 Numerical implementation

We consider an incompressible fluid in a cubical box of length 2π. We solve (1.6) and (1.7) with and without a forcing term, coupled with (2.23) (for the rotation model), using periodic boundary conditions in all three directions. In Fourier space (1.6) and (1.7) may be combined to give (subscript **k** has been dropped)

$$\frac{\partial \widehat{\widetilde{U}}_i}{\partial t} = -\nu k^2 \widehat{\widetilde{U}}_i + \mathcal{P}\left[-(ik_j \widehat{\widetilde{U}_i \widetilde{U}_j}) - (ik_m \widehat{T}_{im}) + \widehat{f}_i\right], \tag{3.1}$$

where $\mathcal{P}$ is the projection operator on the space of solenoidal fields, defined as

$$\mathcal{P} = \delta_{ij} - \frac{k_i k_j}{k^2}. \tag{3.2}$$

In k-space (2.23) is

$$\frac{\partial \widehat{\ell}_i}{\partial t} - ik_j \widehat{\ell_j \widetilde{U}_i} = 0. \tag{3.3}$$

A Fourier-Galerkin pseudo-spectral method is used with '3/2 de-aliasing rule' for the non-linear terms both in the momentum and subgrid equations that is 32 Fourier modes in each direction are advanced in time; the computation of the non-linear terms were done using 48 modes, the extra 16 modes used for padding. A second-order explicit Runge-Kutta scheme is used for time advancement which can be illustrated as follows:

Equation (3.1) can be rewritten in the form,

$$\frac{\partial}{\partial t}\left(e^{\nu k^2 t}\widehat{\widetilde{U}}_i\right) = -e^{\nu k^2 t}\mathcal{P}\widehat{\widetilde{g}}_i(\widehat{\widetilde{\mathbf{U}}}_i) \tag{3.4}$$

where $-\widehat{\widetilde{g}}_i(\widehat{\widetilde{\mathbf{U}}}_i)$ denotes the bracketed term in (3.1). We recall from ordinary differential equations the RK2 template as $dy/dt = h(y,t); k_1 = dt \cdot h(y^n, t^n); k_2 = dt \cdot h(y^n + k_1, t^n + dt); y^{n+1} = y^n + \frac{1}{2}k_1 + \frac{1}{2}k_2$. When applied to equation (3.4) we have,

$$\begin{aligned}
k_1 &= dt \cdot \left(-e^{-\nu k^2 t^n}\mathcal{P}\widehat{\widetilde{g}}_i(\widehat{\widetilde{\mathbf{U}}}_i^{\,n})\right), \\
\widehat{\widetilde{U}}_i^{\,n+1/2} &= e^{-\nu k^2 dt} \cdot \left(\widehat{\widetilde{U}}_i^{\,n} - \mathcal{P}\widehat{\widetilde{g}}_i(\widehat{\widetilde{\mathbf{U}}}_i^{\,n}) \cdot dt\right), \\
k_2 &= dt \cdot \left(-e^{-\nu k^2 t^{n+1}}\mathcal{P}\widehat{\widetilde{g}}_i(\widehat{\widetilde{\mathbf{U}}}_i^{\,n+1/2})\right), \\
\widehat{\widetilde{U}}_i^{\,n+1} &= e^{-\nu k^2 dt} \cdot \left(\widehat{\widetilde{U}}_i^{\,n} - \frac{dt}{2}\mathcal{P}\widehat{\widetilde{g}}_i(\widehat{\widetilde{\mathbf{U}}}_i^{\,n})\right) - \frac{dt}{2}\mathcal{P}\widehat{\widetilde{g}}_i(\widehat{\widetilde{\mathbf{U}}}_i^{\,n+1/2}).
\end{aligned}$$

The rotation model is incorporated into the LES code as follows; equations (1.6), (1.7), (2.15),and (2.23), are solved simultaneously for the fields $\widetilde{U}_i$ and ℓ_i. At a given time-step (or intermediate time-step) the ℓ_i are obtained from the Fourier coefficients $\hat{\ell}_i$ which allows construction of the rotation matrix $\mathsf{E}_{ij}(\mathbf{x})$ and hence the contractions $\widehat{S}_1$ and $\widehat{S}_2$. For the *fixed* $\mathcal{K}_0$ scheme, in which $\mathcal{K}_0$ is a specified parameter, equation (2.29) is solved for X_m individually at each of 32^3 points using Newton-Raphson, whence $\epsilon(\mathbf{x})$ follows from (2.28) and $\tau_{ij}(\mathbf{x})$ from (2.26). This is transformed back to Fourier space and fed into the momentum equation. In the *coupled* $\mathcal{K}_0$ scheme, the scalar solution of (2.29) is replaced by simultaneous solution of (2.34) and (2.37), which gives both $\mathcal{K}_0$ and the dissipation field. We note that the Jacobian of the coupled nonlinear system is diagonal with single sidebands

thus the linear equations which result from application of the Newton-Raphson method can be solved directly in order $M = 32^3$ operations.

The *local alignment* models operate similarly but do not require solution of (2.23) since $\widehat{S}_1$ and $\widehat{S}_2$ can be calculated directly from resolved flow variables. Some extra computation is involved is solving the scalar equation in each cell to obtain the eigenstates of $\widetilde{S}_{ij}$. We used the initial approximation $X = \hat{S}_1^{-1/4}$, $\hat{S}_2 < 0$, and, from dominant balance, $X = 2.0$, $\hat{S}_2 > 0$. This itself can be avoided if (2.32) is used but this was found to produce a somewhat overly dissipative model in the DNS limit; see discussion below. A choice of $\mathcal{K}_0 = 1.5$ is used as an initial guess for flows with $R_\lambda > 80$; for lower Reynolds number one needs to lower this initial guess to obtain convergence. Unless otherwise stated results presented in this chapter are obtained using 32 Fourier modes in each direction.

3.2 The Taylor-Green problem

The Taylor-Green flow (Taylor and Green 1937) develops from a single-mode two-dimensional velocity field and produces small-scale structure by means of vortex stretching. The flow develops from the initial condition (the characteristic velocity and length scales are unity),

$$\begin{aligned} \widetilde{U}(x,y,z,0) &= \sin(x)\cos(y)\cos(z), \\ \widetilde{V}(x,y,z,0) &= -\cos(x)\sin(y)\cos(z), \\ \widetilde{W}(x,y,z,0) &= 0, \end{aligned} \tag{3.5}$$

as shown in Figure 3.1(a-d). The initial time evolution of the flow is inviscid and develops into well organized, symmetric laminar structures in the form of vortex sheets shown in Figure 3.2(a-d). These sheets subsequently roll up to become unstable and lead to fully three dimensional turbulent flow.

We run the simulation until a maximum time of $t = 18$ at a Reynolds number 3000 $(= 1/\nu)$. Figure 3.3(a) shows the evolution of the total kinetic energy. The total energy is almost unaltered until a time $t = 6$. This is the regime where the flow is essentially inviscid owing to the generation of fine scales. After energy has redistributed among the wavenumbers, the flow starts to dissipate as shown in Figure 3.3(b). Figure 3.3(c) shows the Taylor Reynolds number, R_λ, which steadily drops and settles at ~ 70. That the model is

inoperative until $t = 6$ is evidenced by Figure 3.3(d), which shows a plot of the Kolmogorov prefactor, $\mathcal{K}_0$. Figure 3.4 shows the flattening of the energy spectrum and the generation of higher wavenumber modes with increasing time.

Brachet et al. (1983) performed DNS of this flow at an effective resolution of 512^3. Comparisons with their DNS have not been made since their simulations enforce symmetries in the velocity field which are maintained during the course of the run. This is done by representing the velocity field as an appropriate choice of expansion in terms of trigonometric functions. Our spectral method only assumes periodicity in the velocity field.

The Taylor-Green problem highlights an important feature of the C-$\mathcal{K}_0$ scheme. While the flow is essentially fully resolved at early times, the Taylor Reynolds number, R_λ, is high ~ 1000; our models turn off since the C-$\mathcal{K}_0$ scheme enforces continuity of the energy spectrum at the cutoff. Models incorporating the F-$\mathcal{K}_0$ scheme perform poorly in this situation since the value of the Kolmogorov prefactor is specified (and is $\mathcal{O}(1)$) and the X's evaluated in equation (2.29) are not $\mathcal{O}(1)$ since $\widehat{S}_1$ is large. However it should be noted that the Taylor-Green flow is a mathematical artifact and is simply a vehicle for producing decaying turbulence, thus the somewhat poor performance of the F-$\mathcal{K}_0$ scheme is not a serious issue.

3.3 Isotropic turbulence

3.3.1 Decaying turbulence

We study decaying isotropic turbulence in order to compare our results to the experiment of Comte-Bellot and Corrsin (1971). They measured the energy spectrum at three downstream locations in grid turbulence. One can relate this to decaying isotropic turbulence by invoking the Taylor approximation. We mimic their experiment by studying turbulence in a cubical box with periodic boundary conditions. In a frame of reference moving with the mean flow speed,

$$t = \int_0^x \frac{dx'}{\overline{U}(x')} \tag{3.6}$$

where x is the downstream distance from the grid and $\overline{U}(x)$ is the mean flow velocity over the cross-section of the tunnel. We have non-dimensionalized the experimental data by the following characteristic velocity, length and time scales: $U_{ref} = \sqrt{3U_0'^2/2}$, $L_{ref} = L/2\pi$

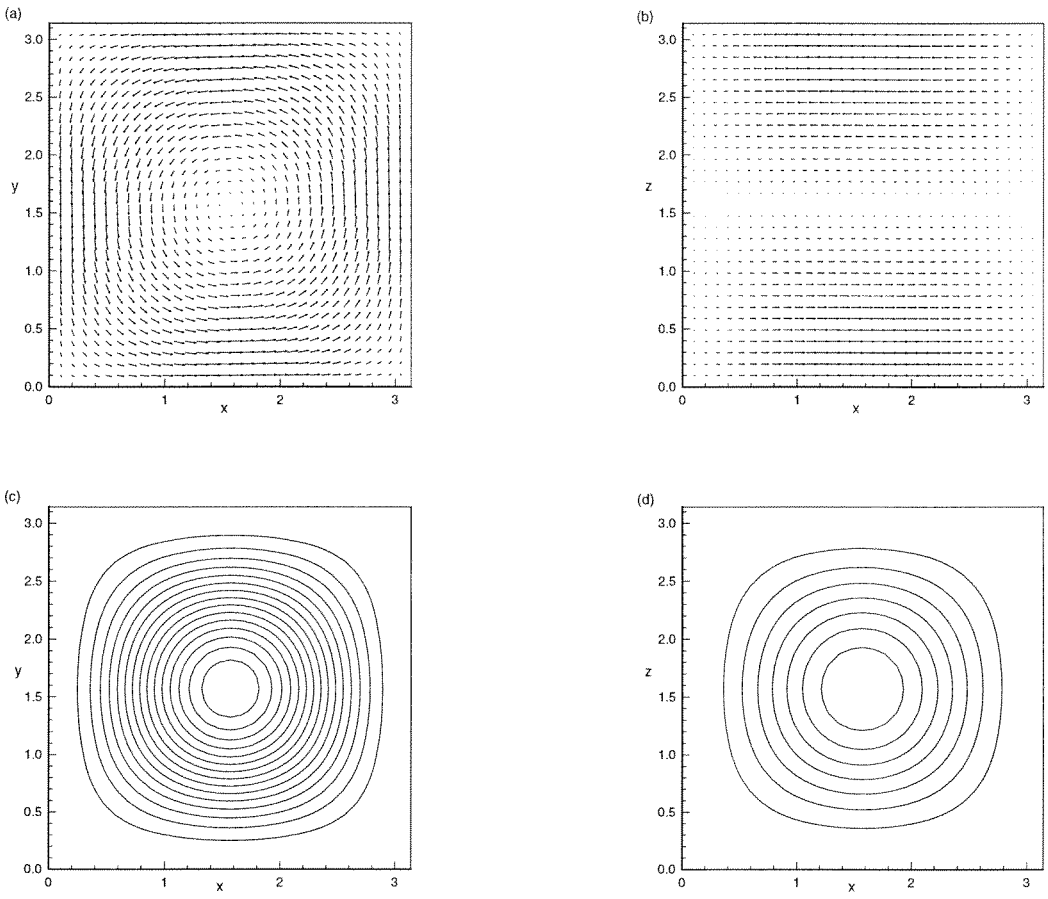

Figure 3.1: The flow configuration at time $t = 0$. (a) and (b) show the velocity vectors while (c) and (d) represent the enstrophy contours in the respective planes.

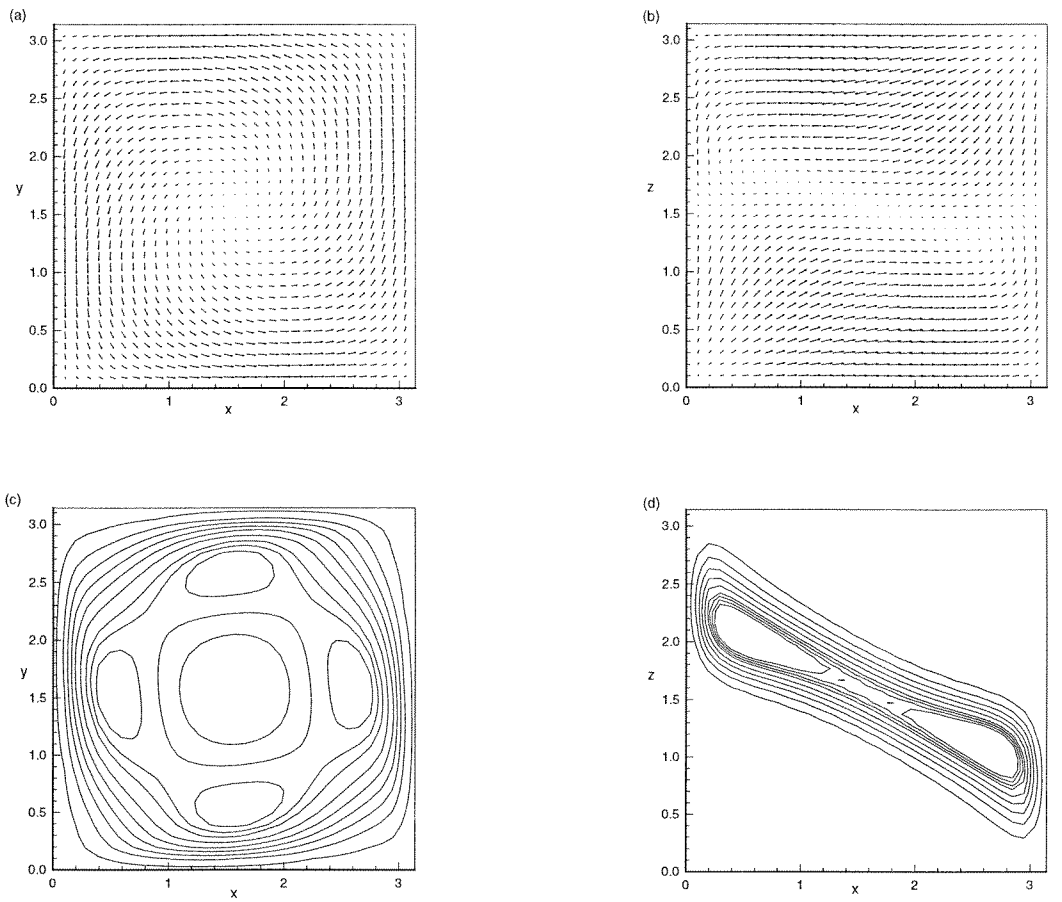

Figure 3.2: The flow configuration at time $t = 2$ using 64^3 modes and with $\nu = 0.01$. (a) and (b) show the velocity vectors while (c) and (d) represent the enstrophy contours in the respective planes.

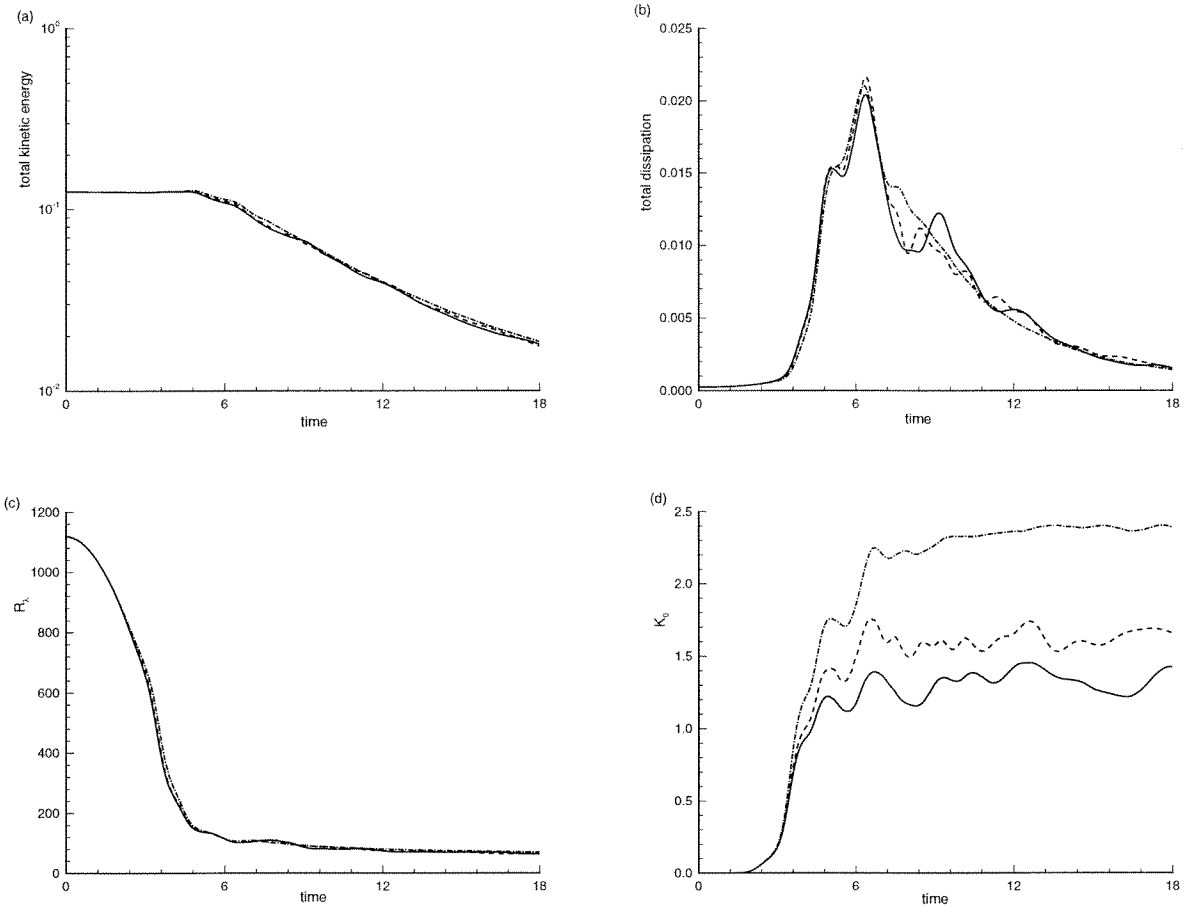

Figure 3.3: Time evolution of (a) kinetic energy (b) total dissipation ($\epsilon = 2\nu\widetilde{S}_{ij}\widetilde{S}_{ij} - \widetilde{S}_{ij}\tau_{ij}$) (c) R_λ and (d) the Kolmogorov prefactor $\mathcal{K}_0$. Solid line - Model 1a, dashed line - Model 1b and dot-dashed lines - Rotation model.

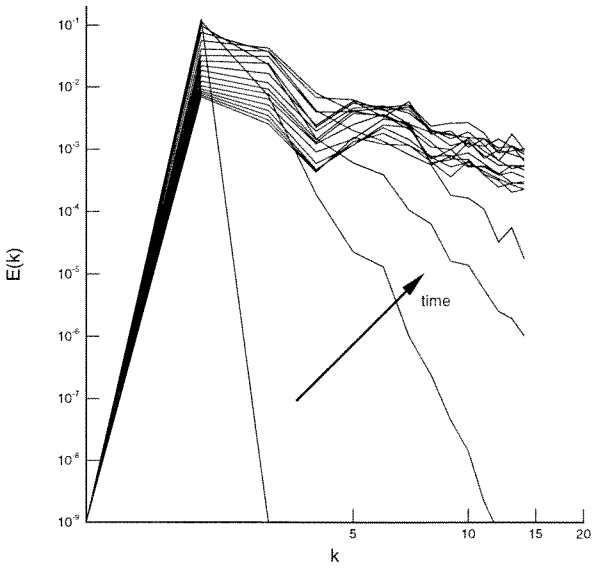

Figure 3.4: Time evolution of the energy spectrum $E(k)$ for Model 1a.

and $t_{ref} = L_{ref}/U_{ref}$. In their experiments the velocity fluctuation at the first measuring station is $\sqrt{U_0'^2} = 22.2$ cm/s, the free-stream speed is $U_\infty = 10^3$ cm/s and the spacing of the turbulence generating mesh is $M_g = 5.08$ cm. The size of the computational box, $L = 11M_g$, was chosen to contain roughly four integral scales. The times at the three stations were measured in terms of $U_\infty t/M_g$. The initial Taylor Reynolds number is $R_\lambda \simeq 80$. In order to compare the resolved and the subgrid part of the turbulent energy produced by the computation, the measured spectra have been integrated over the relevant scale ranges. The initial conditions are generated by the choice of the energy spectrum whence Fourier coefficients with random phases are constructed. This procedure is illustrated in Appendix C.

Figure 3.5(a) shows the decay of the resolved energy with time for all the three models. The dotted line is the result of running the simulation with the model switched off. It is evident that the models play an important role in providing dissipation of kinetic energy. The decay of the subgrid energy with time is shown in Figure 3.5(b). Note that the subgrid energy is obtained from the model without the solution of additional field equations. Since the subgrid energy is derived from knowledge of the resolved field and the chosen subgrid energy spectrum, it cannot be independently initialized to match the experimental value.

Figures 3.6(a-b) compare the resolved energy spectra with the measurements at the initial time and then at the two later instances. The initial spectrum is generated to match the experimental data, while the later two curves are the spectra calculated from the three models. Figure 3.5(a) gives the area under the curve of Figures 3.6(a-b) at the three time instances, over the resolved range of scales. While all models give good agreement with the data for the decay of the resolved energy, C-$\mathcal{K}_0[1a]$ and C-$\mathcal{K}_0[1b;0.5]$ seem to give a slightly better resolved-scale spectrum than C-$\mathcal{K}_0[2]$. This may be related to an observed tendency for the power spectrum of the ℓ_i for the rotation model (not shown) to peak towards the cutoff at k_c followed by a rapid decrease to zero at $k = k_c$. This apparently results from the nonlinear coupling between the ℓ_i and the $\tilde{U}_i$ fields, which in the absence of viscous damping produces a mild cascade towards higher wavenumbers and a subsequent buildup near $k = k_c$. The response of the $\tilde{U}_i$ field is seen to be a concomitant increase in $E(k)$ near the cutoff. The interaction between subgrid structures in adjacent cells occurs only implicitly via the LES equations and the subgrid stress relations. This is apparently too weak to adequately damp high wavenumber growth. Figure 3.7 shows the value of the Kolmogorov prefactor, $\mathcal{K}_0$, with time. The Kolmogorov prefactor $\mathcal{K}_0$ settles to about 1.5 for C-$\mathcal{K}_0[1a]$, 1.85 for C-$\mathcal{K}_0[1b;0.5]$ and hovers around 2.5 for the C-$\mathcal{K}_0[2]$. LES with C-$\mathcal{K}_0[1b]$ for a range of values of μ were performed and yielded satisfactory results in the sense of agreement of the energy decay with experiment; $\mu = 0$ resembled the rotation model in its behavior *vis-à-vis* the energy spectrum and the value of $\mathcal{K}_0$. Results in this thesis will only be presented for the case $\mu = 0.5$.

In order to examine grid dependence, we performed LES with resolution $16^3, 32^3$ and 64^3 respectively for C-$\mathcal{K}_0[1a]$. Figure 3.8 summarizes the performance of the model at the three different resolutions for decaying turbulence in comparison to the results of Comte-Bellot & Corrsin. Since by virtue of (2.25) and (2.9), the subgrid contribution to the total energy is estimated directly, the total turbulent energy can be calculated. This is shown in Figure 3.8(b) from which it may be seen that both the 32^3 and the 64^3 simulations give good agreement with the data. Convergence with respect to increasing N is achieved at $N = 32$. The 16^3 simulation agrees well with the filtered data in Figure 3.8(a) but underestimates the total energy because the cutoff is too near the peak of the energy spectrum to allow the subgrid component to be reasonably well represented by (2.25). The computed spectra, including the subgrid component for $N = 32$, are shown in Figure 3.8(c), while the

dynamically computed $\mathcal{K}_0$ for the three cases is shown in Figure 3.8(d). Tests with C-$\mathcal{K}_0[1b]$ and C-$\mathcal{K}_0[2]$ show that the computed energy decay is quite insensitive to this aspect of the overall model but that the computed $\mathcal{K}_0$ depends on the orientation model.

We remark that models incorporating the C-$\mathcal{K}_0$ scheme have a correction mechanism that takes into account any rise in energy in the high wavenumber modes, i.e., a rise in $\widetilde{E}(\widetilde{k})$ is invariably followed by a rise in the value of $\mathcal{K}_0$, which in turn results in higher dissipation thereby resulting in a drop in $\widetilde{E}(\widetilde{k})$ in the following time-step. In order to test this we performed simulations with no 3/2 de-aliasing but only a spherical truncation. The spherical truncation gets rid of the doubly- and triply-aliased terms but not the singly-aliased terms (Canuto et al. 1987). The results shown in Figure 3.9(a) are only marginally different. Figure 3.9(b) shows the resolved kinetic energy for various cases. Shown are truncated DNS, de-aliased DNS, truncated C-$\mathcal{K}_0$ scheme and de-aliased C-$\mathcal{K}_0$ scheme. It is clear that truncated DNS blows up while the truncated C-$\mathcal{K}_0$ model predicts the right decay rate. We also remark that there is a considerable saving in computational cost with spherical truncation since the evaluation of the non-linear terms require smaller size FFT's in each direction.

The computing time per time-step relative to the Smagorinsky model with constant C was found to be approximately 1.5 for Models 1a and 1b and about 3 for the rotation model. The C-$\mathcal{K}_0$ scheme was marginally more expensive than the F-$\mathcal{K}_0$ scheme.

3.3.2 Forced turbulence

Forcing is achieved by exciting low wavenumbers such that the total energy injection rate is constant in time (Carati et al. 1995). A certain selected number of Fourier modes are chosen from a wavenumber shell $|\mathbf{k}| = k_0$. The Fourier coefficient of the forcing term is then written as,

$$\widehat{\mathbf{f}}_k = \frac{\delta}{N} \frac{\widehat{\widetilde{\mathbf{U}}}_k^*}{|\widehat{\widetilde{\mathbf{U}}}_k|^2} \tag{3.7}$$

for all modes in the specified shell. The above choice of $\widehat{\mathbf{f}}_k$ ensures that the energy injection rate, $\sum \widehat{\mathbf{f}}_k \cdot \widehat{\widetilde{\mathbf{U}}}_k$, is a constant and equal to δ. We have chosen $k_0 = 2, N = 20$ (a box of side 2 grid units centered around the origin with the center modes and the origin left out) and $\delta = 0.1$ for all the runs. LES simulations with forcing were performed over a range of R_λ. The simulations run stably and eventually reach steady-state when statistics

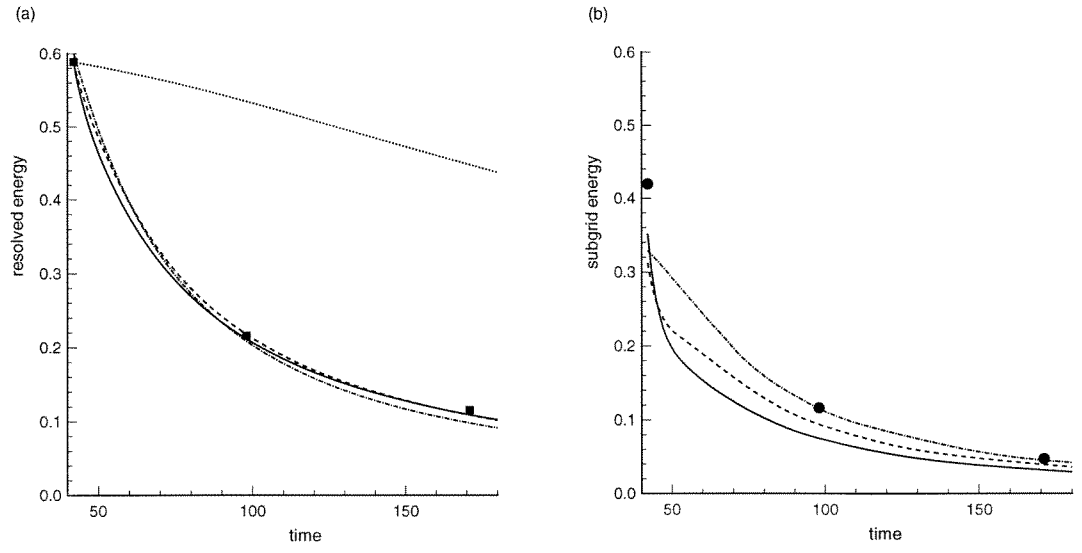

Figure 3.5: Decay of the resolved (a) and the subgrid (b) energy. Solid line - C-$\mathcal{K}_0$[1a], dashed line - C-$\mathcal{K}_0$[1b; 0.5], dot-dashed line - C-$\mathcal{K}_0$[2] and dotted line - no model. The symbols are data from Comte-Bellot & Corrsin (1971).

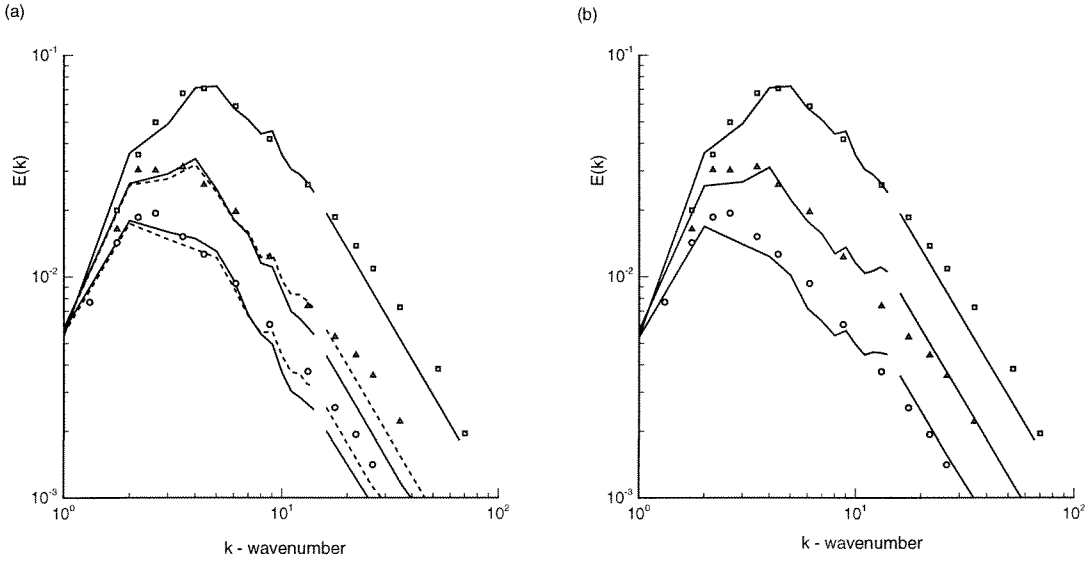

Figure 3.6: Time evolution of spectra in decaying turbulence at three time instances. Solid line - C-$\mathcal{K}_0$[1a] and dashed line - C-$\mathcal{K}_0$[1b; 0.5] (a). C-$\mathcal{K}_0$[2] (b). The symbols are data from Comte-Bellot & Corrsin (1971). The straight lines for $k > k_c$ are the modeled subgrid spectra.

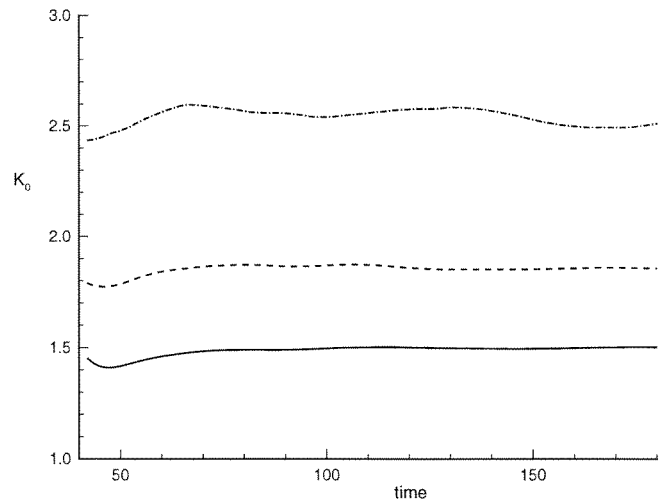

Figure 3.7: Time variation of the Kolmogorov prefactor, $\mathcal{K}_0$, in decaying turbulence. solid line - C-$\mathcal{K}_0$[1a], dashed line - C-$\mathcal{K}_0$[1b; 0.5] and dot-dashed line - C-$\mathcal{K}_0$[2].

are collected. Figure 3.10(a) shows a plot of $\langle \varepsilon_{sgs} \rangle / \langle \epsilon \rangle$, the ratio of the average subgrid dissipation to the total average dissipation in the box versus R_λ. The three curves shown are for the Smagorinsky model, the *fixed* $\mathcal{K}_0$ models and the *coupled* $\mathcal{K}_0$ models. For models incorporating the C-$\mathcal{K}_0$ scheme for forced turbulence, the computed values of $\mathcal{K}_0$ (not shown) showed an R_λ dependence that was somewhat model-dependent. For each model $\mathcal{K}_0$ increased with increasing R_λ from near zero at the DNS limit and reached a plateau for values of R_λ greater than about 100. These asymptotic, large R_λ values were 1.3, 1.5 and 2.0 for C-$\mathcal{K}_0[1a]$, C-$\mathcal{K}_0[1b; 0.5]$ and C-$\mathcal{K}_0[2]$ respectively, which we note are somewhat lower than the values shown in Figure 3.10(a). This appears to be an R_λ effect. For the F-$\mathcal{K}_0$ calculations, these asymptotic $\mathcal{K}_0$ values were used for all R_λ. Figure 3.10(a) shows that the C-$\mathcal{K}_0$ models are less dissipative in the DNS limit than the F-$\mathcal{K}_0$ models and thus are superior in this respect. Figure 3.10(b) is a plot of $k_c\langle\eta\rangle$ versus R_λ where here $\langle\eta\rangle = (\nu^3/\langle\epsilon\rangle)^{1/4}$, $\langle\epsilon\rangle$ being the box-averaged total dissipation. In both figures all results for the three models employing the same scheme were graphically indistinguishable. With 32^3 modes fully resolved DNS can be run at about $R_\lambda \simeq 25$. This was confirmed by turning off the SGS model and comparing computed values for the skewness and the flatness factors of the longitudinal velocity derivatives and one component of the vorticity with the results of Kerr (1985) at the same resolution and similar R_λ. With the SGS models turned on we

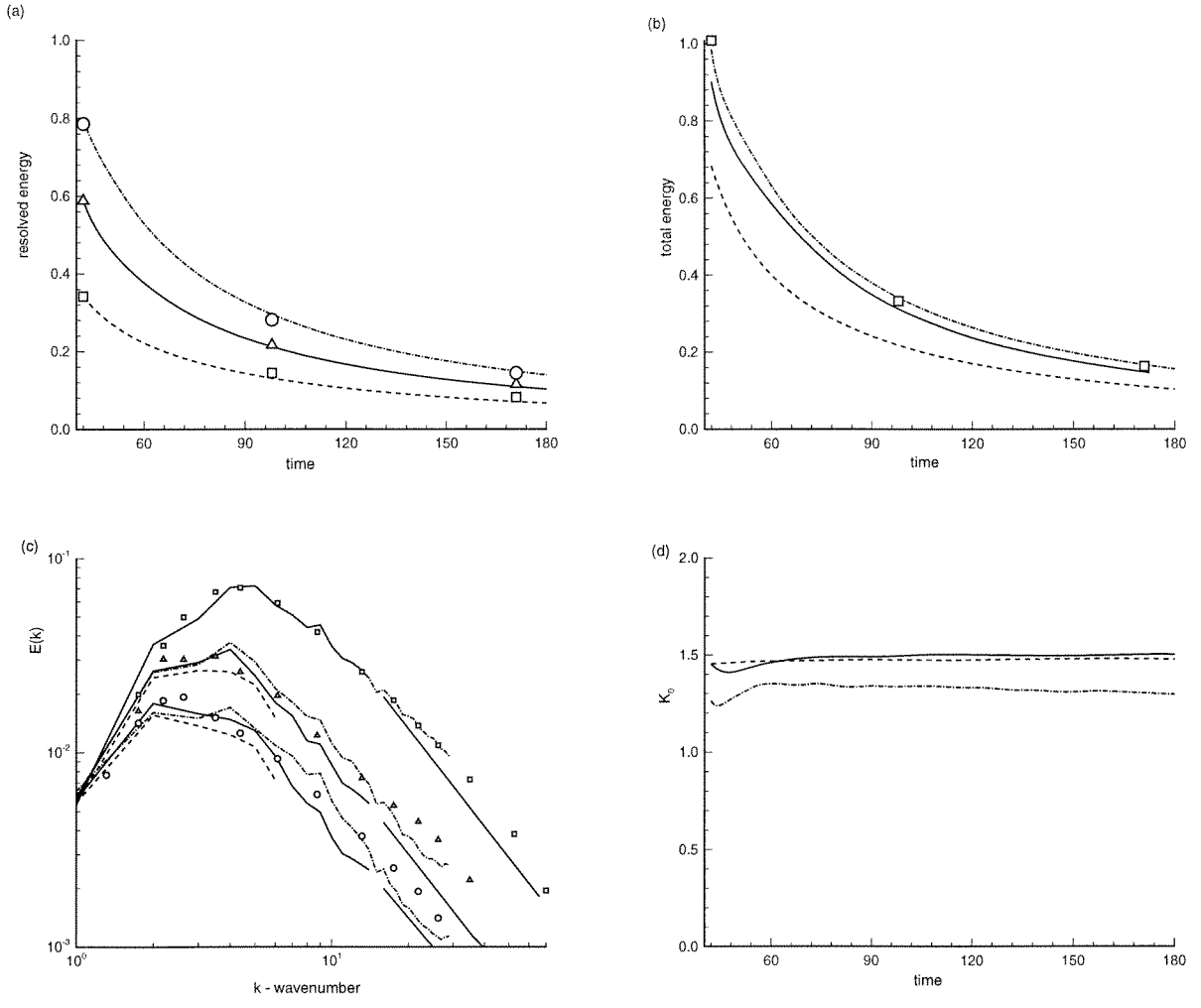

Figure 3.8: Decay of the resolved (a) and total (b) energy for C-$\mathcal{K}_0$[1a]. The energy spectra at three instances are shown in (c). Time variation of the Kolmogorov prefactor is shown in (d). Dashed line - 16^3, solid line - 32^3 and dash-dotted line - 64^3. The symbols are data from Comte-Bellot & Corrsin (1971).

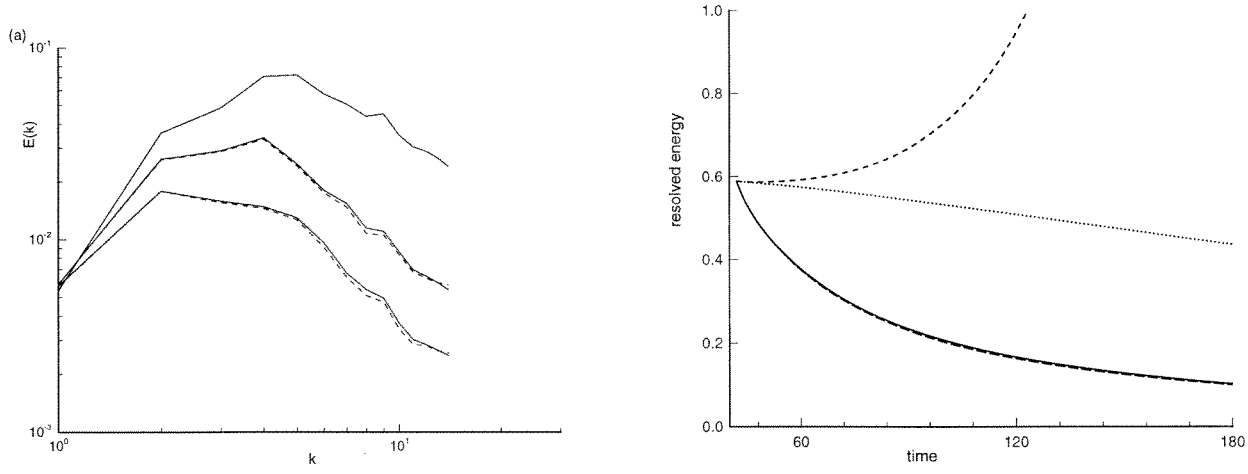

Figure 3.9: Energy spectra with (solid line) and without 3/2 de-aliasing for C-$\mathcal{K}_0$[1a]. The dashed line represents the simulation with only spherical truncation (a). Figure (b) shows the resolved energy for this case. Also shown in Figure (b) are truncated DNS (dashed) and de-aliased DNS (dotted) along with truncated C-$\mathcal{K}_0$[1a] (long-dashed) and de-aliased C-$\mathcal{K}_0$[1a].

find $k_c\langle\eta\rangle = 1$ at $R_\lambda \simeq 25$, indicating near full resolution except in the far viscous range. Figure 3.10(a) shows that the models are subdominant in this DNS limit, providing less than, 0.0003 (C-$\mathcal{K}_0$) and 0.008 (F-$\mathcal{K}_0$), of the volume-averaged dissipation. By comparison, the Smagorinsky model produces a fraction 0.16 of the total dissipation at $R_\lambda \simeq 25$.

We remark that the simplest possible model of the present class can be constructed using vortex alignment with the eigenvector corresponding to λ_3 and (2.32) to evaluate ε_{sgs}. At $R_\lambda \simeq 90$ this model performed similarly to Model 1a for both decaying and homogeneous turbulence and was only marginally slower than Smagorinsky. It was found, like Smagorinsky, to be too dissipative in the DNS limit, and so is not discussed in detail.

The pdf of SGS in filtered DNS fields for both box turbulence (Carati et al. 1995) and non-homogeneous flows (Mason and Thomson 1992) have typically shown some 30% backscatter. It follows from (2.24) that backscatter, defined by $\varepsilon_{sgs} < 0$ occurs whenever $\widehat{S}_2 > 0$ while $\widehat{S}_2 < 0$ gives cascade. A straightforward calculation using (2.24) shows that SGS dissipation can be written as

$$\begin{aligned} \varepsilon_{sgs} &= -K\,\widetilde{S}_{ij}\left(\delta_{ij} - \frac{\ell_i\ell_j}{\ell_m\ell_m}\right) \\ &\sim -\widehat{S}_2\,K, \end{aligned}$$

$$= \tilde{S}'_{33}\, K, \tag{3.8}$$

where $\tilde{S}'_{33}$ is the component of $\tilde{S}_{ij}$ aligned with the vortex. Hence backscatter, defined by $\varepsilon_{sgs} < 0$ occurs whenever $\widehat{S}_2 > 0$ - the SGS vortices are being compressed on the average - while $\widehat{S}_2 > 0$ - the vortices are axially stretched - gives cascade. Figures 3.11(a-c) show scatter plots of $\hat{S}_1$ versus $\hat{S}_2$ for the three orientation models obtained from a simulation at $R_\lambda \simeq 90$. Models incorporating the C-$\mathcal{K}_0$ or the F-$\mathcal{K}_0$ scheme exhibit similar behavior. Model 1a has no backscatter (this can be demonstrated) while Model 1b (with $\mu = 0.5$) shows some ($\sim 3\%$) backscatter. The rotation model shows substantial backscatter, about $\sim 40\%$, and it is possible that this may be related to its somewhat higher computed values of $\mathcal{K}_0$ compared to Model 1a and Model 1b. A simulation with C-$\mathcal{K}_0[1b;0]$, i.e., full alignment with the vorticity, show a similar scatter plot to C-$\mathcal{K}_0[2]$. This suggests a strategy of adjustment of μ to obtain backscatter agreeing with filtered DNS. It is interesting to note that all the points lie within a bounding parabola. An estimate based on a locally two-dimensional 'maximum stretch' scenario for $\hat{S}_{ij}$ gives a bounding parabola $\hat{S}_1 = 16\,\hat{S}_2^2$. We find however that $\hat{S}_1 = 12\,\hat{S}_2^2$ gives a slightly better boundary and so this curve is displayed in the figures. The backscatter properties of the models are also illustrated in Figure 3.12 which shows a pdf of the "stretch," that part of the velocity gradient-tensor which stretches the subgrid vorticity. The stretch is suitably normalized by $\sqrt{\langle\epsilon\rangle/\nu}$. The pdf of the dissipation $\log_{10}\frac{\epsilon}{\langle\epsilon\rangle}$ for the three models is displayed in figure 3.13. The distribution appears to be approximately log-normal.

It was remarked earlier that (2.29) can exhibit regions of multiple roots in the $\hat{S}_2$ versus $\hat{S}_1$ plane, posing a potential problem in obtaining a unique value of ϵ, given $\hat{S}_1, \hat{S}_2$. This can be shown to occur only when $\hat{S}_2 < 0$. The boundary of the region corresponding to multiple-valuedness of $X(\hat{S}_1, \hat{S}_2)$ in the $\hat{S}_1, \hat{S}_2$ plane always lies well away from populated regions of the scatter-plots of Figure 3.11. In fact when $\hat{S}_1 >> 1$ this boundary is given by $\hat{S}_2 \approx -256\hat{S}_1/(81\,\mathcal{K}_0)$ which lies well below the parabola bounding the scatter plots.

Comparisons were made with 128^3 DNS data (Misra and Lund 1996) at $R_\lambda \sim 85$. The data was filtered down to 32^3 to appropriately compare with LES results. Shown in Figure 3.14 is the pdf of the "stretch". It is evident that the rotation model mimics the behavior of filtered DNS fairly well. Plotted on the same graph is F-$\mathcal{K}_0[1b;0.5]$ which exhibits about 5% backscatter. We remark that F-$\mathcal{K}_0[1b;0]$ has a similar peformance as that of the rotation

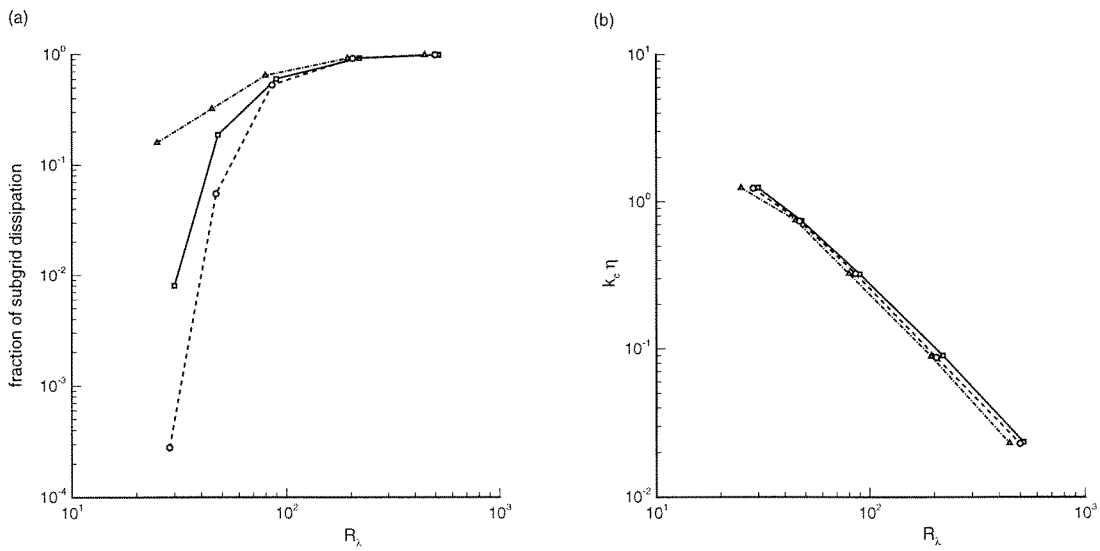

Figure 3.10: $\langle \varepsilon_{sgs} \rangle / \overline{\epsilon}$ versus R_λ (a) and $\langle k_c \eta \rangle$ versus R_λ (b). Solid line - F-$\mathcal{K}_0$ scheme (Models 1a, 1b and 2 are indistinguishable) , dashed line - C-$\mathcal{K}_0$ scheme (Models 1a, 1b and 2 are indistinguishable) and the dot-dashed line - Smagorinsky model with $C = 0.17$.

model. The symbols are data from DNS. The models performed satisfactorily in *a priori* tests, i.e., wherein the $\widetilde{S}_{ij}$ field was extracted from DNS and subjected to the model and appropriate quantities compared with filtered DNS. The correlations of the SGS stresses were roughly 0.4 for the SGS energy, i.e., diagonal components and about 0.1 for the off-diagonal components.

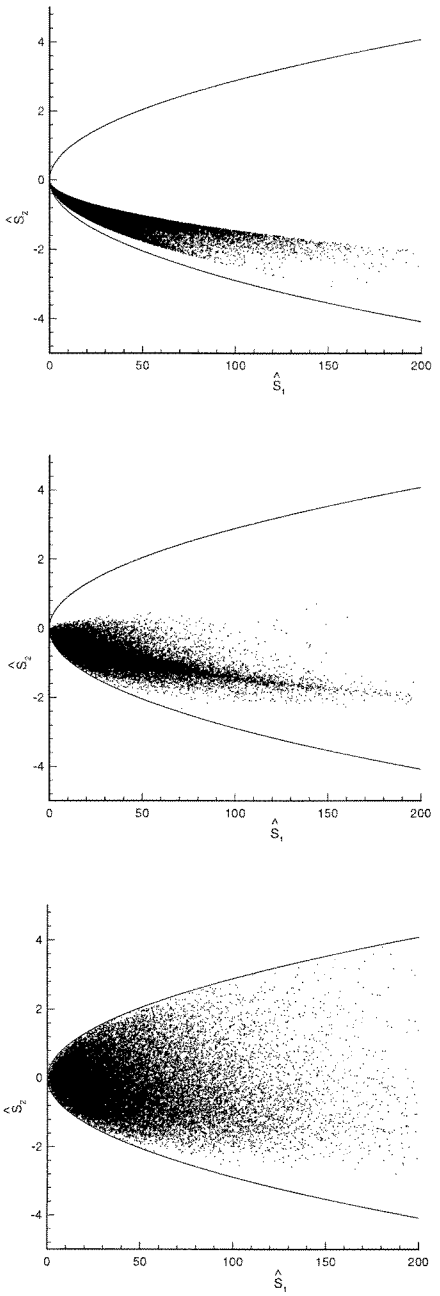

Figure 3.11: Scatter plot of $\hat{S}_1$ versus $\hat{S}_2$ indicating regions of backscatter. F-$\mathcal{K}_0$[1a] (top, a) shows no backscatter, F-$\mathcal{K}_0$[1b; 0.5] (middle, b) shows some backscatter and F-$\mathcal{K}_0$[2] (bottom, c) shows about 40% backscatter. C-$\mathcal{K}_0$ models exhibit similar behavior.

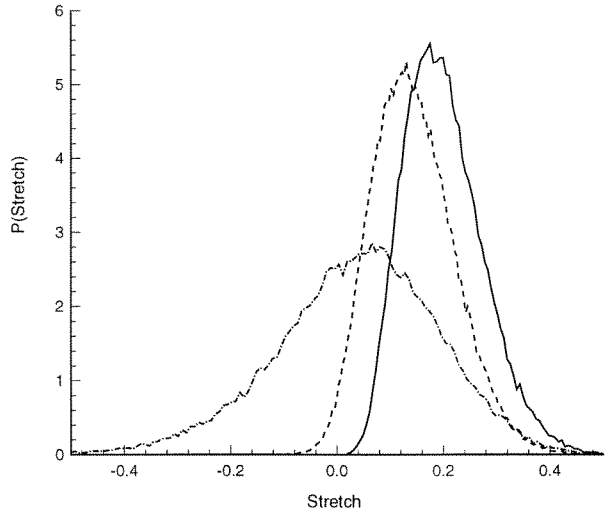

Figure 3.12: pdf of the "stretch" - $\omega_i' \ \partial\tilde{U}_i/\partial x_j \ \omega_j'$. Solid line - F-$\mathcal{K}_0$[1a], dashed line - F-$\mathcal{K}_0$[1b; 0.5] and dot-dashed line - F-$\mathcal{K}_0$[2]. C-$\mathcal{K}_0$ models exhibit similar behavior.

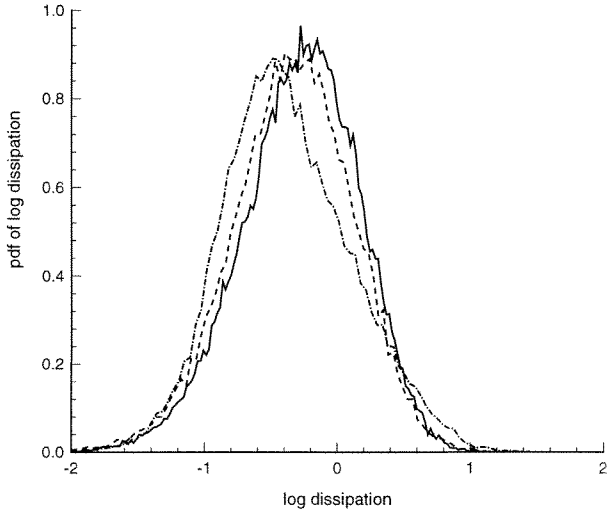

Figure 3.13: pdf of the $\log_{10}\frac{\epsilon}{\langle\epsilon\rangle}$. Solid line - C-$\mathcal{K}_0$[1a], dashed line - C-$\mathcal{K}_0$[1b; 0.5] and dot-dashed line - C-$\mathcal{K}_0$[2]. F-$\mathcal{K}_0$ models exhibit similar behavior.

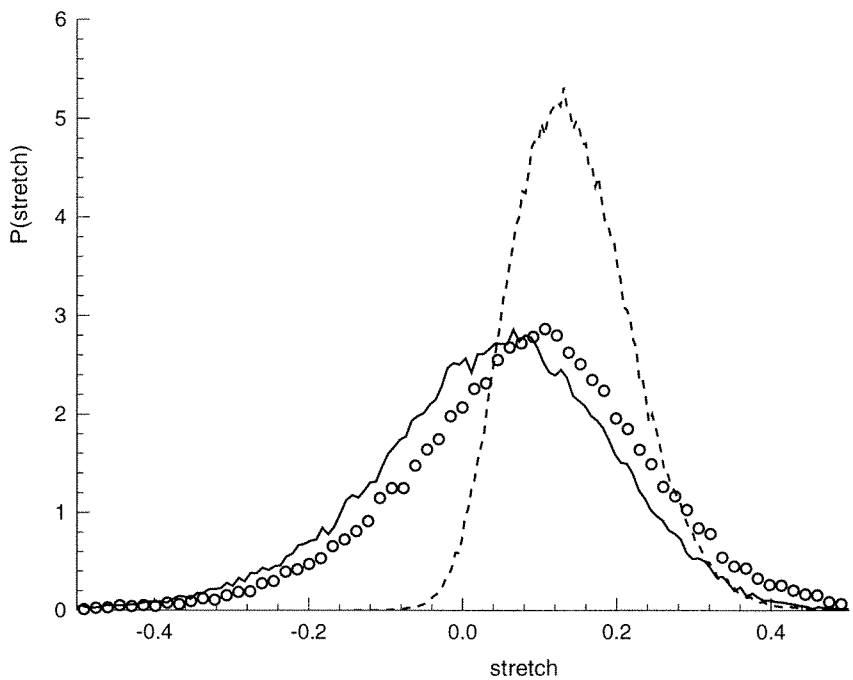

Figure 3.14: pdf of the "stretch". Solid line is F-$\mathcal{K}_0[2]$ and the dashed line is F-$\mathcal{K}_0[1b; 0.5]$. Symbols are data from DNS.

Chapter 4

Inhomogeneous flows - three-dimensional channel flow

In order to test the stretched-vortex models in inhomogeneous flows, we perform LES of turbulent channel flow. This is chosen due to its geometric simplicity and the extensive documentation of experimental and DNS data. We consider a three-dimensional channel with the fluid contained between two parallel rigid walls separated by a distance L_z in the wall-normal direction (z). The channel is of length L_x in the streamwise direction (x) and L_y in the spanwise direction (y). We non-dimensionalize the governing equations by the channel half-width ($\delta = L_z/2$) as the length scale and the friction velocity ($u_\tau = (\tau_w/\rho)^{1/2}$) as the velocity scale. We further decompose the pressure into a mean pressure gradient driving the flow and a fluctuating component. The choice of the non-dimensionalization ensures a mean pressure gradient of -1. Thus the governing equations in non dimensional form may be written as,

$$\frac{\partial \widetilde{U}_i}{\partial x_i} = 0, \tag{4.1}$$

$$\frac{\partial \widetilde{U}_i}{\partial t} + \frac{\partial}{\partial x_j}\left(\widetilde{U}_i \widetilde{U}_j\right) = -\left(\frac{\partial \widetilde{p}}{\partial x_i} - \delta_{i1}\right) - \frac{\partial T_{ij}}{\partial x_j} + \frac{1}{R_\tau}\frac{\partial^2 \widetilde{U}_i}{\partial x_j \partial x_j}, \tag{4.2}$$

where, $R_\tau = u_\tau \delta/\nu$, is the Reynolds number. In this chapter we will consider the flow with $R_\tau = 180$ with the channel dimensions $4\pi \times 2\pi \times 2$ at a grid resolution $32 \times 32 \times 65$. Based on the grid resolution and the domain size, $\Delta x_+ \simeq 70$ and $\Delta y_+ \simeq 35$, where the subscript "+" denotes the distance in wall units defined by, $\Delta x_+ = u_\tau \Delta x/\nu$. There are 5 points in the wall-normal direction which reside in the viscous sublayer, $z_+ \sim 12$; the closest away from the wall being at $\Delta z_+ \simeq 0.3$.

4.1 Numerical implementation

We incorporate the spectral code developed by Chan (1996). The code uses a pseudo-spectral numerical method in the spatial direction with Fourier expansions in the streamwise

and spanwise directions and Legendre polynomials in the wall-normal direction. While details of the code can be found in Chan (1996), we present here a brief description of the code and its implementation in LES using our model.

4.1.1 Temporal integration

The equations are integrated in time using an operator splitting procedure developed by Moin and Kim (1982) wherein the convection, diffusion and the pressure gradient terms are treated separately. The net effect of such a procedure is to integrate the filtered momentum equations as a series of scalar partial differential equations. In the first step, the convection and the SGS terms are integrated explicitly using a four-step Runge-Kutta method; this is followed by an implicit treatment of the viscous term using the Crank-Nicolson scheme. The intermediate velocity obtained from these steps, in general is not divergence free, therefore the last step aims to adjust the pressure gradient in order to make the final velocity field divergence free.

The Runge-Kutta scheme when applied to the convection and the subgrid terms yields

$$\begin{aligned}
\widetilde{\mathbf{U}}^0 &= \widetilde{\mathbf{U}}^n \\
\widetilde{\mathbf{U}}^1 &= \widetilde{\mathbf{U}}^n + \delta t \alpha_1 H^0 \\
\widetilde{\mathbf{U}}^2 &= \widetilde{\mathbf{U}}^n + \delta t \alpha_2 H^1 \\
\widetilde{\mathbf{U}}^3 &= \widetilde{\mathbf{U}}^n + \delta t \alpha_3 H^2
\end{aligned}$$

$$\widetilde{\mathbf{U}}^p = \widetilde{\mathbf{U}}^n + \delta t \alpha_4 H^3 \tag{4.3}$$

where, $\alpha_1 = \frac{1}{4}$, $\alpha_2 = \frac{1}{3}$, $\alpha_3 = \frac{1}{2}$ and $\alpha_4 = 1.0$

$$H = \frac{1}{2}(\nabla \cdot (\widetilde{\mathbf{U}}\widetilde{\mathbf{U}}) + \widetilde{\mathbf{U}} \cdot \nabla \widetilde{\mathbf{U}}) + \nabla \cdot \mathbf{T} \tag{4.4}$$

where $\mathbf{T}$ is the subgrid-stress tensor. The code employs the skew-symmetric form for the convective terms in order to control the aliasing errors.

The Crank-Nicolson scheme, when applied to the viscous terms in the second step, gives

an intermediate velocity as

$$\frac{\widetilde{\mathbf{U}}^* - \widetilde{\mathbf{U}}^p}{\delta t} - \frac{1}{2}\frac{1}{R_\tau}\nabla\cdot\nabla(\widetilde{\mathbf{U}}^* + \widetilde{\mathbf{U}}^n) = 0 \tag{4.5}$$

this solution procedure requires a boundary condition for $\widetilde{\mathbf{U}}^*$. If the no-slip condition is applied along a solid boundary, the overall accuracy of the above scheme is only first-order in time. As a remedy, Kim and Moin (1985) derive an extrapolation procedure that will recover the second-order accuracy. The boundary condition for $\widetilde{\mathbf{U}}^*$ then becomes

$$\widetilde{\mathbf{U}}^* = \widetilde{\mathbf{U}}^{n+1} + \delta t\nabla\phi^{n-1}. \tag{4.6}$$

The resulting velocity, $\widetilde{\mathbf{U}}^*$, in general, will not satisfy the continuity equation and is corrected as

$$\widetilde{\mathbf{U}}^{n+1} = \widetilde{\mathbf{U}}^* - \delta t\nabla\phi^n \tag{4.7}$$

where ϕ is a auxiliary scalar variable. By imposing the continuity condition on the new velocity field, one obtains

$$\nabla\cdot\nabla\phi^n = \frac{\nabla\cdot\widetilde{\mathbf{U}}^*}{\delta t}. \tag{4.8}$$

4.1.2 Spatial discretization

The flow has two homogeneous directions and thus periodic boundary conditions are assumed in the streamwise and spanwise directions. Following a Galerkin spectral formulation, we can write (4.5) as

$$\int[\frac{2}{\delta t} + \frac{1}{R_\tau}(k_x^2 + k_y^2)]\widehat{\widetilde{\mathbf{U}}}^{n+\frac{1}{2}}\ W\ d\Gamma - \int\frac{1}{R_\tau}\frac{\partial^2\widehat{\widetilde{\mathbf{U}}}^{n+\frac{1}{2}}}{\partial z^2}\ W\ d\Gamma = \int(\frac{\widehat{\widetilde{\mathbf{U}}}^n + \widehat{\widetilde{\mathbf{U}}}^p}{\delta t})\ W\ d\Gamma \tag{4.9}$$

where, Γ is taken to be a set of non-overlapping elements filling the space in the vertical direction, W is a weighting function and

$$\widehat{\widetilde{\mathbf{U}}}^{n+\frac{1}{2}} = 0.5\ (\widehat{\widetilde{\mathbf{U}}}^* + \widehat{\widetilde{\mathbf{U}}}^n).$$

For details on W see Chan (1996).

Similarly the third fractional time step may be written as,

$$\int W(k_x^2+k_y^2)\widehat{\phi}\,d\Gamma - \int \frac{\partial W}{\partial z}\frac{\partial \widehat{\phi}}{\partial z}\,d\Gamma = \delta t\left(\int W(ik_x\widehat{\widetilde{U}}^* + ik_y\widehat{\widetilde{V}}^*)\,d\Gamma + \int \frac{\partial W}{\partial z}\widehat{\widetilde{W}}^*\,d\Gamma\right) + Ww|_{z=0}^{z=H} - W\frac{\partial \phi}{\partial z}|_{z=0}^{z=H}$$

where $\widehat{\widetilde{U}}^*$, $\widehat{\widetilde{V}}^*$, and $\widehat{\widetilde{W}}^*$ are the velocity components in the x, y and z directions respectively. Due to the compatibility condition that is required for the solution of a Poisson equation, the last two terms of the above equation cancel each other. Thus no artificial boundary conditions are required for ϕ.

Spatial integration is performed using the Gauss quadrature rule. For example,

$$\int_{-1}^{1} f d\xi = \sum_{k=o}^{N} g_k f(\xi_k)$$

where g_k is the weighting factor defined as

$$g_k = \frac{2}{N(N+1)}\frac{1}{[L_N(\xi_k)]^2}$$

where, ξ_k are the Legendre-Gauss-Lobatto points and L_k is the kth order Legendre polynomial.

The solution procedures marches forward in time as three different integration steps. For the first step, we integrate the convective terms using a four-stage Runge-Kutta scheme, this is followed by the Crank-Nicolson scheme for the viscous terms and a fully implicit scheme for the pressure gradient term. We evaluate a set of non-linear operators for the Runge-Kutta scheme and solve a set of Helmholtz equations for both the viscous and pressure terms.

Each stage of the Runge-Kutta step requires the evaluation of 16 spatial derivatives in the horizontal directions, 8 spatial derivatives in the vertical direction, 16 inverse Fourier transforms and 17 forward Fourier transforms.

4.1.3 SGS model implementation

We presently implement only models incorporating the C-$\mathcal{K}_0$ scheme for reasons to be discussed in the next section. The implementation details of the C-$\mathcal{K}_0$ scheme is similar to

that described in the earlier chapter with changes required by the presence of inhomogeneity in the wall-normal direction.

Equations (2.34) and (2.37) are solved in planes normal to the wall while equation (2.35) is now obtained by considering a two-dimensional energy spectrum. Hence when following the method described in §2.3 for dynamically computing $\mathcal{K}_0$, the two-dimensional energy spectrum, $\tilde{E}_{2D}(\mathrm{K})$, of the resolved flow in $x-y$-planes, where $\mathrm{K}^2 = k_x^2 + k_y^2$, was matched to the $x-y$-plane average of the equivalent two-dimensional subgrid spectrum. Under the assumption that the shell-summed subgrid spectrum is of the form (2.35), we show in Appendix D, that for a single vortex structure whose axis makes an angle α with the z direction, this two-dimensional subgrid spectrum takes the form

$$E(\mathrm{K}) = \mathcal{K}_0 Q(\alpha)\, \epsilon^{2/3}\, \mathrm{K}^{-5/3}, \tag{4.10}$$

where $Q(\alpha)$ is a correction factor in the range $0.7319 < Q \leq 1$ which can be calculated numerically as a function of α and stored as a table look-up. For the channel flow, at fixed z, both Q and ϵ are functions of x and y. Hence presently, when matching (4.10) to the two-dimensional resolved spectrum computed from the resolved flow in planes $z = \mathrm{Const}$, Q and ϵ are replaced by their $x-y$ plane averaged values. This has the consequence that the dynamic calculation of $\mathcal{K}_0$ takes place separately in each of the N_z planes, and so $\mathcal{K}_0 = \mathcal{K}_0(z)$. The computational penalty for this is small.

Two other features of the model implementation method are worth noting, first the cutoff wavenumber, k_c, is defined as $k_c = \pi/\Delta$, where Δ is chosen as the Deardorff formula i.e. $(\Delta x \Delta y \Delta z)^{1/3}$. Second, in order to reduce computation we solve for K only at the first fractional time step of the four-step Runge-Kutta scheme, while the vortex orientations are determined from the $\tilde{S}_{ij}$ field at all the intermediate steps. This also has the added effect of keeping the divergences small in the calculation.

Comparisons will be made with the Smagorinsky model with $\Delta = (\Delta x \Delta y \Delta z)^{1/3}$ and $C = 0.1$ as defined in (1.10). In order to achieve lower dissipation near the walls, the length scale, Δ, is reduced using the Van Driest damping function (Moin and Kim 1982).

4.2 Results and discussion

The simulations were run until a statistical steady-state was achieved, and for an additional 10 eddy-turnover times during which statistics were collected. Figure 4.1 shows the normalized wall shear stress. The wall shear oscillates about its steady averaged value, R_τ, indicating statistical steady-state. As mentioned in §4.1, the temporal marching of the code is performed using a time-splitting procedure which does not strictly enforce the divergence free condition. We plot in Figure 4.2 the absolute value of the maximum divergence defects $(\nabla \cdot \widetilde{\mathbf{U}})$ in each plane. The divergence defects fall off rapidly to zero away from the wall. Since they are $\mathcal{O}(0.1)$ near the wall where the gradients are $\mathcal{O}(R_\tau)$ we are led to believe that the code is accurate to $\mathcal{O}(10^{-3})$. This is somewhat unsatisfactory and is solely a consequence of the time-splitting scheme. However, since the SGS model is inoperative in the near wall region (as will be demonstrated) this may not be a serious issue.

The mean streamwise velocity is shown in Figure 4.3. Shown are two models C-$\mathcal{K}_0[1b;1]$ and C-$\mathcal{K}_0[1a]$ along with under-resolved DNS, the Smagorinsky model and fully resolved DNS of Kim et al. (1987). Both the models do a bit better than the Smagorinsky model but still over-predict the velocity near the center of the channel. The root mean square (rms) quantities are shown in Figure 4.4(a) for both the models. Since the symbols are data from DNS and have not been filtered, we include the subgrid component. If U is the total velocity, then one can show that,

$$\begin{aligned} u_{rms}^2 &= \overline{\left(U - \overline{U}\right)^2} \\ &= \overline{U^2} - \overline{U}^2 \\ &= \overline{\left(\widetilde{U} + u'\right)^2} - \overline{\left(\widetilde{U} + u'\right)}^2 \\ &= \overline{\widetilde{U}^2} - \overline{\widetilde{U}}^2 + \overline{u'^2} \end{aligned}$$

where, $\overline{\text{“ ”}}$ denotes a time average and $\widetilde{\text{“ ”}}$ denotes a spatial average. The last term is the subgrid energy which we include with the resolved quantity. It is seen that the models do fairly well in the streamwise and spanwise rms distributions but w_{rms} predicts a steeper slope. This could be a result of the model being somewhat dissipative in the near-wall region. Figure 4.4(b) shows the time averaged Reynolds stress for the two models. Figures 4.5(a-d) shows the decomposition of the rms and Reynolds stress into the resolved part and

the total component for the C-$\mathcal{K}_0$[1a; 1] model. The difference between them is the SGS contribution.

Figure 4.6 shows the Kolmogorov prefactor versus $z_+ = u_\tau z/\nu$, for the two models. As one would expect, the value of $\mathcal{K}_0$ is almost zero in the near-wall region and rises to values $\mathcal{O}(1)$ in the center of the channel. These values of $\mathcal{K}_0$ are consistent with those established in homogeneous turbulence for the respective models. To establish the contribution of the SGS model to the total dissipation, we plot in Figure 4.7(a), the ratio $\varepsilon_{sgs}/\epsilon$, which is plane averaged. Near the wall, since the Kolmogorov prefactor is small there is no SGS dissipation and ε_{sgs} is expectedly zero. This appears to arise from the part of the model computation that couples the assumed subgrid spectrum to the resolved $(x-y)$-plane 2D spectrum near the cutoff. It seems that there is little turbulent energy in the resolved scales at the cutoff available for transfer to the local subgrid spectrum. The model detects this and responds by producing very small $\mathcal{K}_0$ and ε_{sgs}, thereby effectively shutting itself down. Computed values of $\mathcal{K}_0$ at the wall are $\mathcal{O}(10^{-4})$. We also remark that the flow is almost fully resolved in the vertical direction and we thus expect little contribution from the model. Figure 4.7(b) shows a plot of the plane averaged $X = k_c\eta$. The figure shows that the value of X is not close to unity as one would expect and as was demonstrated in Figure 3.10(b) for homogeneous turbulence. We believe this problem stems from the value of k_c which was chosen using the Deardorff estimate for Δ. This is an *ad hoc* criterion and may not be the appropriate choice. Near the wall, the cells are pancake-like, thus an appropriate choice of the k_c should probably take into account the aspect ratio of the cells. In this study we maintain our choice for k_c while acknowledging this problem. The model nonetheless produces negligible dissipation near the wall since $\mathcal{K}_0$ is small. The *fixed* $\mathcal{K}_0$ scheme will admittedly not work in such a scenario. Both models considered here show the same trend with regard to Figure 4.7. Shown in the figure are results from C-$\mathcal{K}_0$[1b;1].

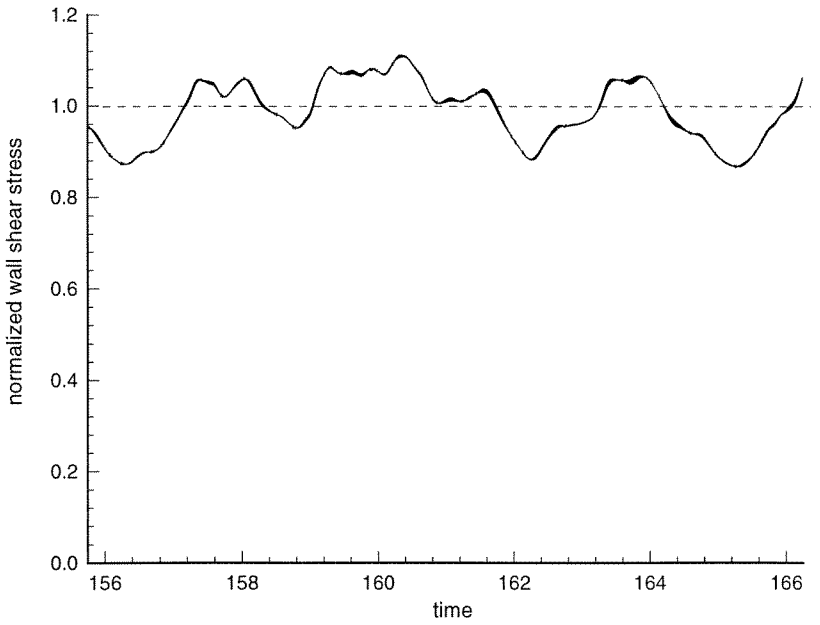

Figure 4.1: The wall shear stress τ_w normalized by R_τ (a). Statistics are collected during this interval.

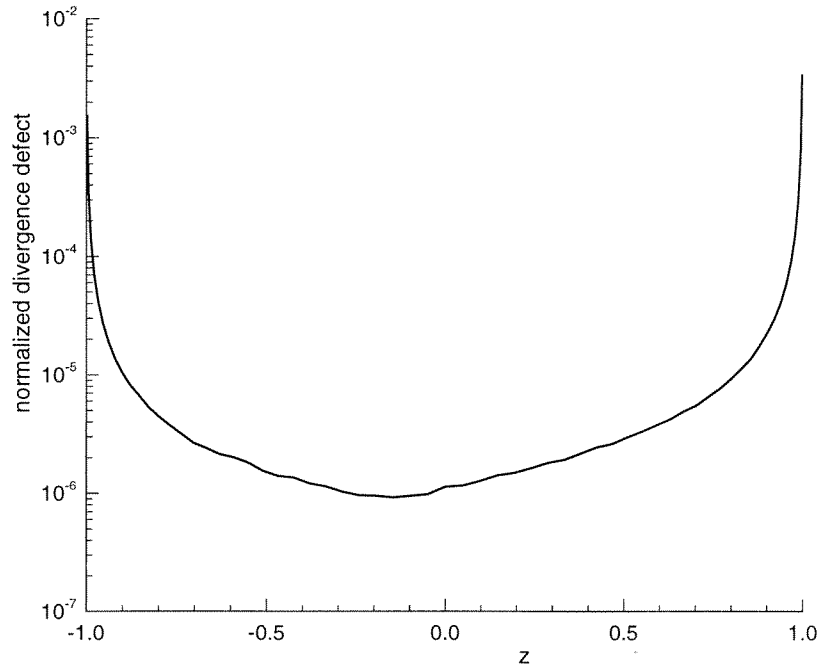

Figure 4.2: Normalized divergence defects in the channel versus channel height.

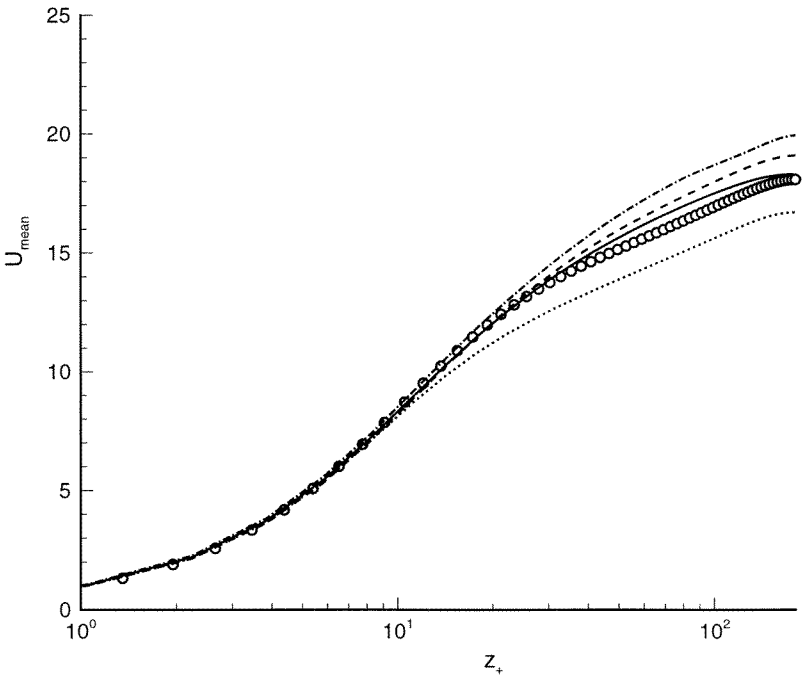

Figure 4.3: Mean streamwise velocity (a). Symbols are data from Kim, Moin & Moser (1987). Solid line is the C-$\mathcal{K}_0[1b;1]$, dashed line C-$\mathcal{K}_0[1a]$, dotted line is under resolved DNS and the dashed-dotted line is the Smagorinsky model with Van Driest wall damping.

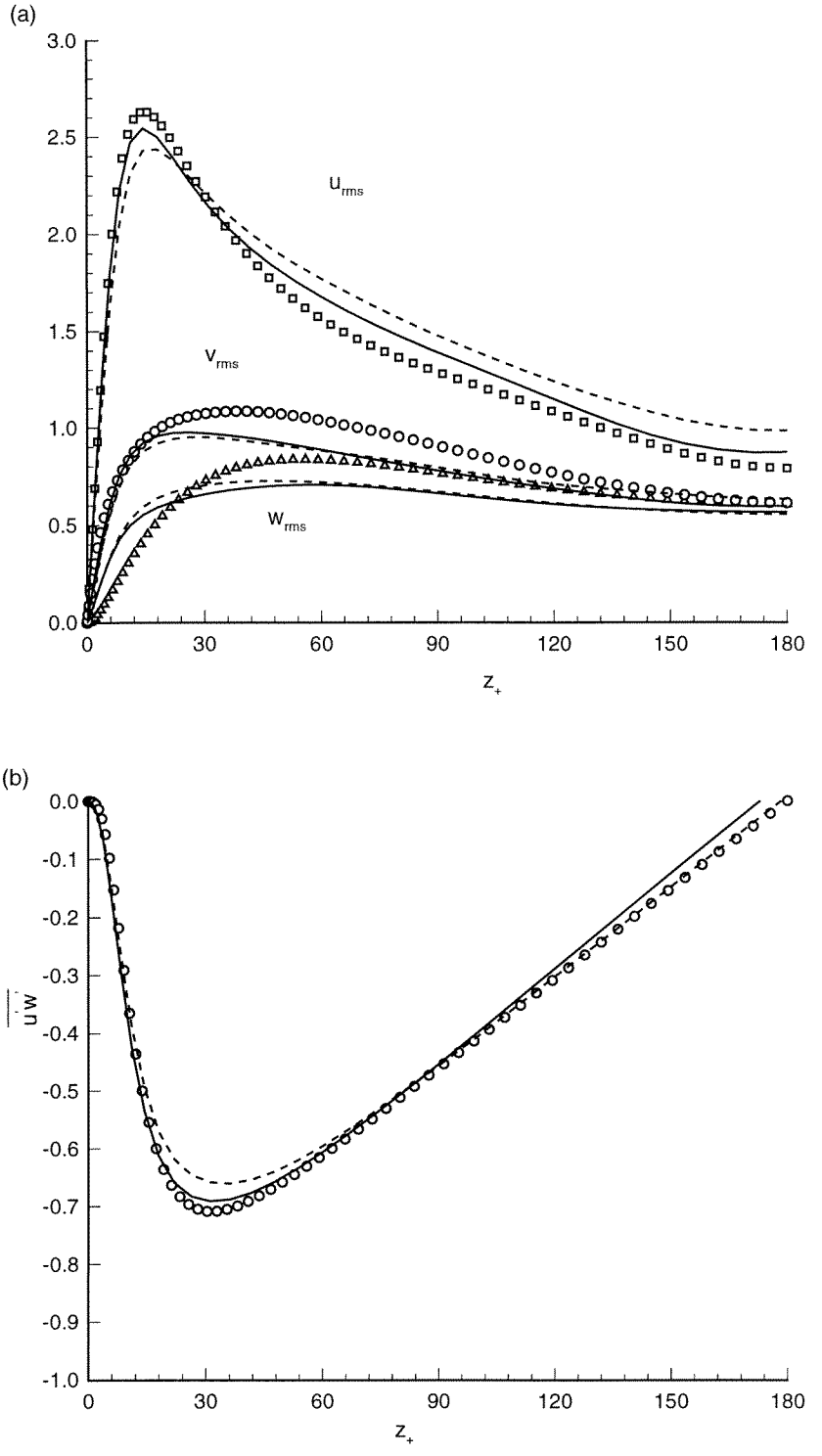

Figure 4.4: Figure (a) shows the rms quantities, while Figure (b) is a plot of the Reynolds stresses, $\overline{u'w'}$. Solid line is the C-$\mathcal{K}_0[1b;1]$, dashed line C-$\mathcal{K}_0[1a]$. The symbols are data from Kim, Moin & Moser (1987).

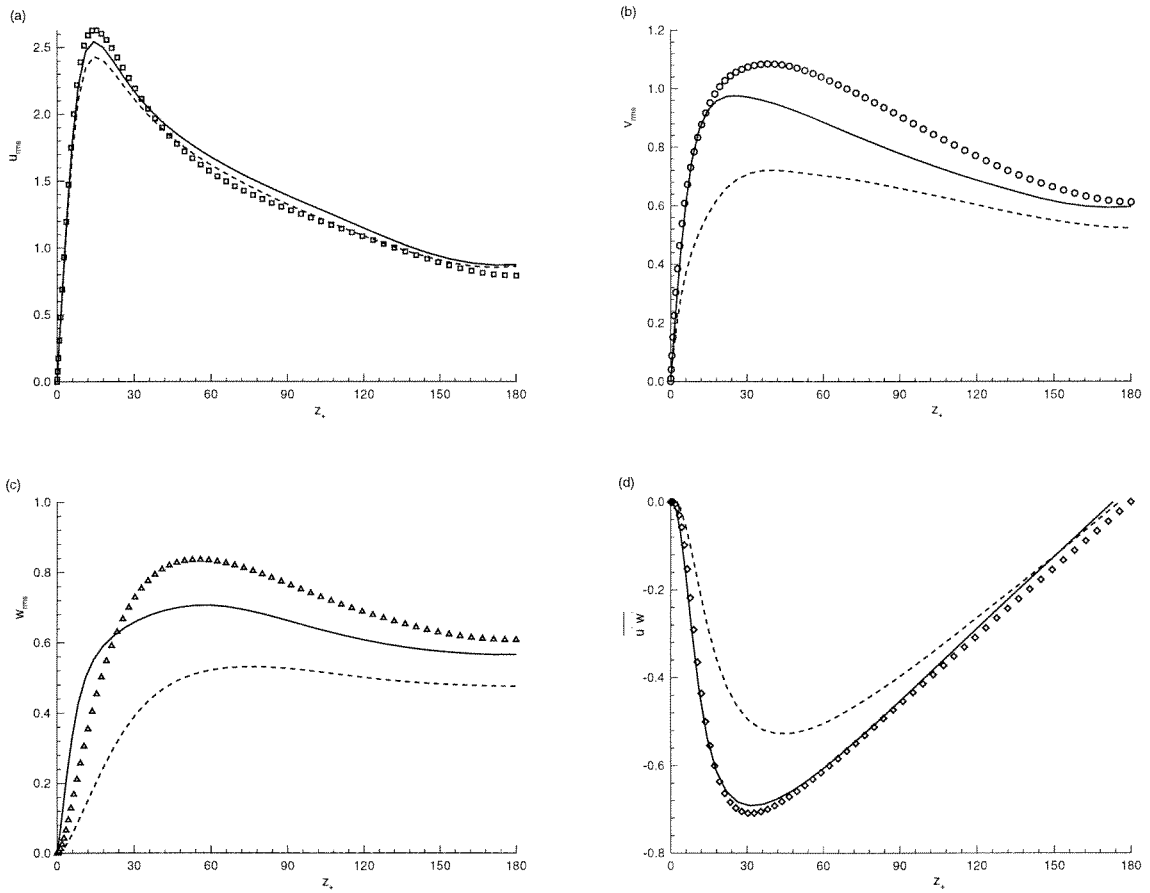

Figure 4.5: (a) u_{rms} (b) v_{rms} (c) w_{rms} and (d) Reynolds stress $\overline{u'w'}$ for C-$\mathcal{K}_0[1b;1]$. Solid line is the total component while dashed line is the resolved part. Symbols are data from Kim, Moin & Moser (1987).

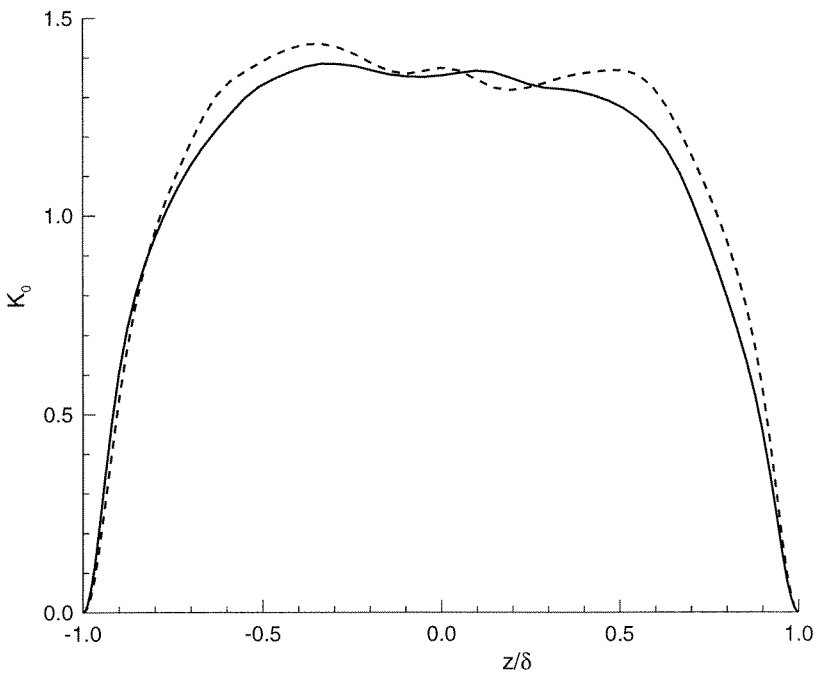

Figure 4.6: The Kolmogorov prefactor for C-$\mathcal{K}_0[1b;1]$ (solid line) and C-$\mathcal{K}_0[1a]$ (dashed line).

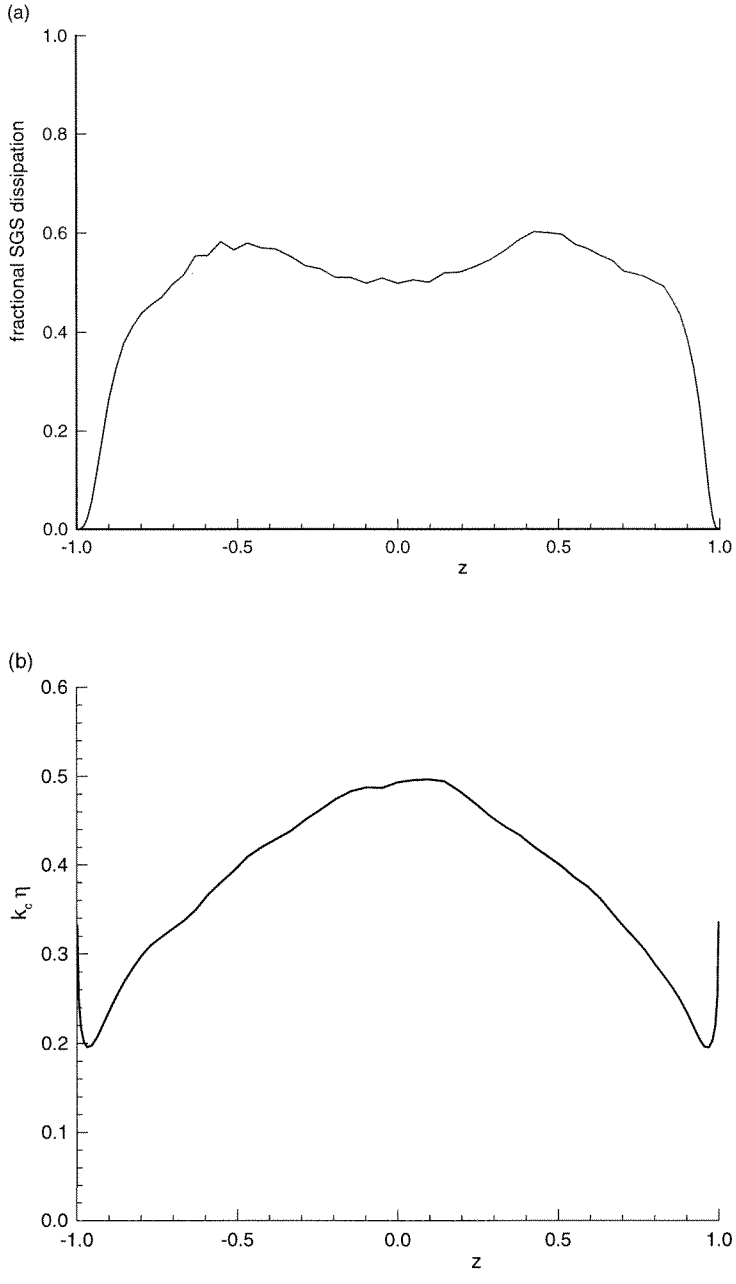

Figure 4.7: Plane averaged $\langle \varepsilon_{sgs}/\epsilon \rangle$ (a) and $\langle k_c \eta \rangle$ (b). This is obtained from a typical data file and is not time averaged. Shown in this figure is C-$\mathcal{K}_0$[1b;1].

Chapter 5

Conclusions and future work

5.1 Conclusions

Stretched-vortex SGS models have been shown to perform well for both decaying and forced isotropic turbulence, over a range of R_λ. They give the subgrid energy directly and appear to produce the correct fully resolved flow in the DNS limit with computational penalty, for the alignment models, of some 25% in comparison to the standard Smagorinsky model. The F-$\mathcal{K}_0$ models are simple to implement and give satisfactory performance. The C-$\mathcal{K}_0$ approach allows dynamic calculation of $\mathcal{K}_0$ at the expense of some extra complexity. All variations of the model tested presently gave good comparison with data for decaying turbulence. The stretched-vortex models have been shown to produce backscatter, but none of the three tested give , in a natural way, the 30% backscatter seen in filtered DNS of isotropic turbulence. At the expense of adjusting μ, the fraction of subgrid vortices aligned with the resolved vorticity, a two-vortex alignment model with the right properties could be constructed but we have not done so presently. We remark that models incorporating the F-$\mathcal{K}_0$ scheme are fully constructed in physical space and thus are amenable to finite difference computations with complex flow geometries.

For the case of the channel flow, the model performed satisfactorily. The *coupled* $\mathcal{K}_0$ model is applied in planes in the wall-normal direction by considering a two-dimensional energy spectrum to estimate the Kolmogorov prefactor. The mean and the rms quantities gave fair agreement the DNS data. The models are about $25 - 50\%$ slower than the Smagorinsky model and are easy to implement.

The stretched-vortex ansatz appears able to give a self-consistent if approximate quantitative description of the detailed fine-scale properties of turbulence and at the same time provides a basis for the construction of workable SGS models relating the averaged behavior of the fine scales to the resolved-flow variables in large-eddy simulation.

5.2 Future work

One could replace the local balance model of Section IIC, including the assumption of a Kolmogorov energy spectrum, with transport equations for the subgrid vortex itself. The relevant equations for the subgrid energy K and the subgrid dissipation ϵ_{sgs} arising from internal SGS vortex motions can be obtained from a model of a vortex evolving in a linear background field (see appendix)

$$\begin{aligned} \frac{DK}{Dt} &= -\widetilde{S}_{ij}\tau_{ij} - \epsilon_{sgs}, \\ &= -K\,\widetilde{S}_{ij}\left(\delta_{ij} - \frac{\ell_i\ell_j}{\ell_m\ell_m}\right) - \epsilon_{sgs} \\ &= \widetilde{S}'_{33}K - \epsilon_{sgs} \end{aligned} \tag{5.1}$$

and

$$\frac{D\epsilon_{sgs}}{Dt} = 2\frac{\ell_i\ell_j}{\ell_k\ell_k}\,\widetilde{S}_{ij}\epsilon_{sgs} - 4\nu^2\int_{k_c}^{\infty} k^4\,E(k)\,dk. \tag{5.2}$$

where ϵ_{sgs} is

$$\epsilon_{sgs} \equiv 2\nu\int_{k_c}^{\infty} k^2\,E(k)\,dk. \tag{5.3}$$

The first term on the right of (5.2) gives the increase of the subgrid enstrophy, and hence the dissipation, produced by local vortex stretching provided by the resolved scales, while the second term gives the effect of viscous diffusion of enstrophy. These equations can replace the local balance model for the computation of K; the stresses are still given by (2.15). The $K - \epsilon_{sgs}$ are not closed however, since $E(k)$ appears in (5.2). Closure can be obtained by applying a time filter to (5.1)-(5.2) and using the well-known approximate relation between the skewness S_3, or dimensionless triple velocity derivative, and $E(k)$, which can be written in the form

$$4\nu^2\int_{k_c}^{\infty} k^4\,E(k)\,dk = -\frac{35}{(15)^{3/2}}S_3\nu^{-1/2}\epsilon_{sgs}^{3/2}. \tag{5.4}$$

Experiment indicates a value near $S_3 = -0.5$. Use of (5.4) in (5.2) with this value gives closure. It may be objected that this is still a one-parameter model, but unlike the Kolmogorov prefactor, S_3 is a defined (model independent) quantity characteristic of the dissipation range of turbulence which by definition, lies outside the range of resolved scales in LES. Some input from experiment or theory is then justified.

Future work on the channel involves designing models that are easier to apply in physical

space. The present C-$\mathcal{K}_0$ scheme is implemented in Fourier space but this method could be used in physical space by replacing (2.35) with its second-order structure function equivalent

$$\overline{(\Delta u)^2} = f\,\mathcal{K}_0\,\epsilon^{2/3}\,r^{2/3}, \tag{5.5}$$

where $\overline{(\Delta u)^2}$ is a measure of the shell-averaged (physical space) longitudinal velocity difference squared, and where $f = 1.31512$. This could be applied either globally with $\epsilon^{2/3}$ replaced by $\langle\epsilon^{2/3}\rangle$ or locally with $r = \Delta$, where Δ is the local node spacing. The implementation of a $K - \epsilon_{sgs}$ version of the vortex model, and the application of the present class of vortex SGS models to complex geometry flows such as a backward facing step, flow past an aerofoil and a myriad other flows of engineering interest provide topics for future research.

Bibliography

Ashurst, W., A. Kerstein, R. Kerr, and C. Gibson (1987). Alignment of vorticity and scalar-gradient in simulated Navier-Stokes turbulence. *Phys. Fluids 30*, 2343–2353.

Bardina, J., J. Ferziger, and W. Reynolds (1980). Improved subgrid model for large-eddy simulation. *AIAA Paper 80-1357.*

Batchelor, G. (1953). *The theory of homogeneous turbulence.* Cambridge University Press.

Bayly, B. (1992). *Infinitely conducting dynamos and other horrible eigenproblems*, Volume 40 of *Nonlinear Phenomena in Atmospheric and Oceanic Sciences*, pp. 139–176. Springer-Verlag.

Brachet, M., D. Meiron, S. Orszag, B. Nickel, R. Morf, and U. Frisch (1983). Small-scale structure of the Taylor-Green vortex. *J. Fluid Mech. 130*, 411–452.

Canuto, C., M. Hussaini, A. Quarteroni, and T. Zang (1987). *Spectral methods in fluid dynamics.* Springer Verlag.

Carati, D., S. Ghosal, and P. Moin (1995). On the representation of backscatter in dynamic localization models. *Phys. Fluids 7(3)*, 606.

Chan, D. C. (1996). *Effects of rotation on turbulent convection: Direct numerical simulatin using parallel processors.* Ph. D. thesis, University of Southern California.

Cocke, W. (1969). Turbulent hydrodynamic line stretching - consequences of isotropy. *Phys. Fluids 12*, 2488.

Comte-Bellot, G. and S. Corrsin (1971). Simple Eulerian time correlation of full and narrow-band velocity signals in grid-generated 'isotropic' turbulence. *J. Fluid Mech. 48*, 273–337.

Domaradzki, J. and E. Saiki (1996). A subgrid-scale model based on the estimation of unresolved scales of turbulence. Technical Report CMS-96-9, University of Southern California.

Germano, M., U. Piomelli, P. Moin, and W. Cabott (1991). A dynamic subgrid scale eddy-viscosity model. *Phys. Fluids A 3*, 1760.

Ghosal, S., T. Lund, P. Moin, and K. Akselvoll (1995). A dynamic localization model for large-eddy simulation of turbulent flows. *J. Fluid Mech. 286*, 229.

Huang, M.-J. (1994). *Theoretical and computational studies of isotropic homogeneous turbulence.* Ph. D. thesis, California Institute of Technology.

Jeffreys, H. and B. Jeffreys (1950). *Methods of Mathematical Physics.* Cambridge University Press.

Kerr, R. (1985). Higher-order derivative correlations and the alignment of small-scale structures in isotropic numerical turbulence. *J. Fluid Mech. 153*, 31–58.

Kida, S. (1981). Motion of an elliptic vortex in a uniform shear flow. *J. Phys. Soc. Japan 50 No. 10*, 3517.

Kida, S. and Y. Murakami (1987). Kolmogorov similarity in freely decaying turbulence. *Phys. Fluids 30*, 2030.

Kim, J. and P. Moin (1985). Application of a fractional-step method to incompressible Navier-Stokes equations. *J. Comp. Phys. 59(2)*, 308–323.

Kim, J., P. Moin, and R. Moser (1987). Turbulence statistics in fully developed channel flow at low Reynolds number. *J. Fluid Mech. 177*, 133–166.

Kraichnan, R. (1976). Eddy viscosity in two and three dimensions. *J. Atmos. Sci. 33*, 1521–1536.

Landau, L. and E. Lifshitz (1959). *Fluid mechanics.* Pergamon Press.

Leonard, A. (1974). Energy cascade in large-eddy simulations of turbulent fluid flows. *Advances in Geophysics 18A*, 237–248.

Leonard, A. (1997). Large-eddy simulation of chaotic advection and beyond. *AIAA Paper 97-024.*

Lesieur, M. and O. Metais (1996). New trends in large-eddy simulation. *Ann. Rev. of Fluid Mechanics 28*, 45–82.

Lundgren, T. (1982). Strained spiral vortex model for turbulent fine structure. *Phys. Fluids 25*, 2193–2203.

Mason, P. and D. Thomson (1992). Stochastic backscatter in large-eddy simulation of boundary layers. *J. Fluid Mech. 242*, 51.

McComb, W. (1990). *The Physics of fluid Turbulence.* Oxford University Press.

Metais, O. and M. Lesieur (1992). Spectral large-eddy simulations of isotropic and stably-stratified turbulence. *J. Fluid Mech. 239*, 157–194.

Misra, A. and T. Lund (1996). Evaluation of a vortex-based subgrid stress model using DNS databases. In *Studying Turbulence using Numerical Simulation Databases - VI*, Proc. of the 1996 Summer Program, Center for Turbulence Research, pp. 359–366.

Misra, A. and D. Pullin (1997). A vortex-based subgrid stress model for large-eddy simulation. *Phys. Fluids (To appear).*

Moin, P. and J. Kim (1982). Numerical investigation of turbulent channel flow. *J. Fluid Mech. 118*, 341–377.

Neu, J. (1984). The dynamics of a columnar vortex in an imposed strain. *Phys. Fluids 27(10)*, 2397.

Orszag, S. (1970). Comments on: Turbulent hydrodynamic line stretching - consequences of isotropy, by W.J. Cocke. *Phys. Fluids 13*, 2203.

Pullin, D., J. Buntine, and P. Saffman (1994). On the spectrum of a stretched spiral vortex. *Phys. Fluids 6*, 3010–3027.

Pullin, D. and P. Saffman (1993). On the Lundgren-Townsend model of turbulent fine scales. *Phys. Fluids A 5*, 126–145.

Pullin, D. and P. Saffman (1994). Reynolds stresses and one-dimensional spectra for a vortex model of homogeneous anisotropic turbulence. *Phys. Fluids 6*, 1787–1796.

Reynolds, O. (1895). On the dynamical theory of incompressible viscous fluids and the determination of the criterion. *Phil. Trans. R. Soc. A 186*, 123.

Reynolds, W. (1992). Towards a structure-based turbulence model. In T. Gatski et al. (Eds.), *Studies in Turbulence*, pp. 76. Springer Verlag.

Reynolds, W. and S. Kassinos (1995). One-point modeling of rapidly deformed homogeneous turbulence. *Proc. R. Soc. Lond. A 451*, 87–104.

Reynolds, W. C. (1989). The potential and limitations of direct and large-eddy simulations. In J. L. Lumley (Ed.), *Whither Turbulence? Turbulence at the Crossroads*, pp. 313. Springer Verlag.

Rogallo, R. S. and P. Moin (1984). Numerical simulation of turbulent flows. *Ann. Rev. of Fluid Mechanics 16*, 99–137.

Saddoughi, S. and S. Veeravalli (1994). Local isotropy in turbulent boundary layers at high Reynolds number. *J. Fluid Mech. 268*, 333.

Smagorinsky, J. (1963). General circulation experiments with primitive equations. *Mon. Weather Rev. 91*, 99.

Spalding, D. and B. Launder (1972). *Lectures in mathematical models of turbulence.* Academic Press.

Taylor, G. and A. Green (1937). Mechanism of the production of the small eddies from large ones. *Proc. R. Soc. London A 158*, 449.

Townsend, A. A. (1951). On the fine-scale structure of turbulence. *Proc. R . Soc. Lond. A 208*, 534.

Vincent, A. and M. Meneguzzi (1991). The spatial structure and statistical properties of homogeneous turbulence. *J. Fluid Mech. 225*, 1–20.

Appendix A

The ellipsoidal pdf model

An attempt was made to numerically solve (2.11) directly, based on the idea of an *ellipsoidal* model pdf. Assume that, at some initial time, $P(\alpha, \beta)$ takes the form of an ellipsoid in the space of the variables defined by $r_1 = \cos\alpha$, $r_2 = \sin\alpha\cos\beta$, $r_3 = \sin\alpha\sin\beta$. This is to be interpreted such that P is given by the cube of the distance from the origin in (r_1, r_2, r_3)-space to the surface of the ellipsoid. Let the principal radii of the ellipsoid be (a_1, a_2, a_3) and let (θ, ϕ, ψ) be the three Euler angles describing the rotation from a coordinate system fixed by the principal axes of the ellipsoid to (r_1, r_2, r_3) axes. Normalization of P requires $a_1 a_2 a_3 = 1$. If P is ellipsoidal initially, then evolution according to (2.11) preserves this geometrical property. Thus (2.11) can be rewritten in terms of six partial differential equations describing the rate of change of the six variables $(a_1, a_2, a_3, \theta, \phi, \psi)$. These are

$$\frac{Da_1}{Dt} = a_1 \widetilde{A}'_{11}, \tag{A.1}$$

$$\frac{Da_2}{Dt} = a_2 \widetilde{A}'_{22}, \tag{A.2}$$

$$\frac{Da_3}{Dt} = a_3 \widetilde{A}'_{33}, \tag{A.3}$$

$$\frac{D\theta}{Dt} = \sin\psi\, \widetilde{B}'_{23} + \cos\psi\, \widetilde{B}'_{31}, \tag{A.4}$$

$$\frac{D\phi}{Dt} = -\frac{\cos\psi}{\sin\theta}\, \widetilde{B}'_{23} + \frac{\sin\psi}{\sin\theta}\, \widetilde{B}'_{31}, \tag{A.5}$$

$$\frac{D\psi}{Dt} = \widetilde{B}'_{12} + \cot\theta\, \cos\psi\, \widetilde{B}'_{23} - \cot\theta\, \sin\psi\, \widetilde{B}'_{31}. \tag{A.6}$$

where,

$$\frac{D}{Dt} = \frac{\partial}{\partial t} + \widetilde{U_j}\,\frac{\partial}{\partial x_j},$$

$$\widetilde{\mathbf{A}}' = \mathsf{E}\,\widetilde{\mathbf{A}}\,\mathsf{E}^{\mathbf{T}}, \tag{A.7}$$

$$\widetilde{B}'_{ij} = \frac{a_j^2\widetilde{A}'_{ij} + a_i^2\widetilde{A}'_{ji}}{a_i^2 - a_j^2}, \tag{A.8}$$

where a prime denotes the frame of the principal axes of the ellipsoid. It may be shown by reconstruction of the ellipsoidal pdf from $(a_1, a_2, a_3, \theta, \phi, \psi)$, that (A1-A6) satisfy (2.11). In the principal-axes frame, the moments reduce to a diagonal tensor for which a look-up table can be prepared. The shear stresses may be calculated given the subgrid kinetic energy. Thus closure is obtained.

Attempts to implement the *ellipsoidal model* failed. It can be shown that the ellipsoidal model is analogous to the motion and deformation of the surface of a material ellipsoid embedded in an evolving velocity-gradient field, and in fact this analogy can be used to obtain (A1-A6). In numerical experiments based on (A1-A6) it was found that the ellipsoid rapidly evolved into a "cigar" irrespective of its initial conditions. This is consistent with the analysis of Cocke (1969) and later Orszag (1970), who showed that for homogeneous isotropic turbulence the length of a material line always increases on the average with time. This lead us to the natural choice of delta-function pdf models.

The derivation of (A1-A6) follows from the close analogy of this problem to that of the motion of a material ellipsoid in an arbitrary strain field. Consider the ellipsoid in the frame of reference of its principal axes. The motion of any material point is given by the equation, $\dot{x'_1} = \widetilde{A}'_{ij}x'_j$. For small time one can do a Taylor series expansion and write,

$$x'_i(t) = x'_i(0) + t\,\widetilde{A}'_{ij}\,x'_j(0) + \mathcal{O}(t^2). \tag{A.9}$$

Thus,

$$r'(t)^2 = x'_i(t)\,x'_i(t) = x'_i(0)^2 + 2\,t\,x'_i(0)\,\widetilde{A}'_{ij}\,x'_j(0) + \mathcal{O}(t^2). \tag{A.10}$$

We can describe points locally about a_1 and construct, for small α, the following parame-

terization.

$$\begin{aligned} x_1'(0) &= r'(0)\,(1-\alpha^2/2), \\ x_2'(0) &= r'(0)\,\alpha\,\cos\beta, \\ x_3'(0) &= r'(0)\,\alpha\,\sin\beta. \end{aligned} \tag{A.11}$$

We now need to evaluate $r'(0)$. We know that,

$$\frac{x_1'(0)^2}{a_1^2} + \frac{x_2'(0)^2}{a_2^2} + \frac{x_3'(0)^2}{a_3^2} = 1. \tag{A.12}$$

Substituting A.11 in A.12 it follows,

$$r'(0) = a_1 \left(1 + \frac{\alpha^2}{2}\,F\right), \tag{A.13}$$

where $F = 1 - \left(a_1^2/a_2^2\right)\cos^2\beta - \left(a_1^2/a_3^2\right)\sin^2\beta$. Therefore we obtain,

$$\begin{aligned} x_1'(0) &= a_1 \left(1 + \frac{\alpha^2}{2}(F-1)\right), \\ x_2'(0) &= a_1\,\alpha\,\cos\beta, \\ x_3'(0) &= a_1\,\alpha\,\sin\beta. \end{aligned} \tag{A.14}$$

Since we need a maximum of $r'(t)$ with respect to α and β, we need to evaluate α and β satisfying the two equations,

$$\frac{\partial r'(t)}{\partial \alpha} = 0\ ;\ \frac{\partial r'(t)}{\partial \beta} = 0. \tag{A.15}$$

Therefore differentiating A.10 with respect to α and β, evaluating α and β for which $r'(t)$ is a maximum and substituting back into A.10 yields,

$$r'(t)^2 = a_1^2 + 2\,a_1^2\,\widetilde{A}_{11}'\,t. \tag{A.16}$$

Therefore,

$$\dot{a_1} = \frac{r'(t) - a_1}{t} = a_1\,\widetilde{A}_{11}'.$$

From symmetry the other two equations are,

$$\begin{aligned} \dot{a_2} &= a_2\, \widetilde{A}'_{22}, \\ \dot{a_3} &= a_3\, \widetilde{A}'_{33}. \end{aligned}$$

Now we need to obtain the rotation rates. From A.9 we can evaluate the coordinates of the material point corresponding to the maximum at time t. They are,

$$\begin{aligned} x'_1(t) &= a_1 + a_1\, \widetilde{A}'_{11}\, t, \\ x'_2(t) &= a_1\, \widetilde{B}'_{12}\, t, \\ x'_3(t) &= a_1\, \widetilde{B}'_{13}\, t. \end{aligned} \tag{A.17}$$

We define the new axes system as,

$$\begin{aligned} x''_1(t) &= a_1\, (1 + \widetilde{A}'_{11}\, t), \\ x''_2(t) &= 0, \\ x''_3(t) &= 0. \end{aligned} \tag{A.18}$$

Thus,

$$x''_i(t) = \mathsf{E}_{ij}(\theta + \Delta\theta, \phi + \Delta\phi, \psi + \Delta\psi)\; \mathsf{E}_{pj}(\theta, \phi, \psi)\; x'_p(t). \tag{A.19}$$

However,

$$\begin{aligned} &\mathsf{E}_{ij}(\theta + \Delta\theta, \phi + \Delta\phi, \psi + \Delta\psi) = \mathsf{E}_{ij}(\theta, \phi, \psi) + \\ &\quad \frac{\partial}{\partial\phi}\mathsf{E}_{ij}(\theta, \phi, \psi)\; \Delta\phi \;+\; \frac{\partial}{\partial\theta}\mathsf{E}_{ij}(\theta, \phi, \psi)\; \Delta\theta \;+\; \frac{\partial}{\partial\psi}\mathsf{E}_{ij}(\theta, \phi, \psi)\; \Delta\psi. \end{aligned} \tag{A.20}$$

Let $G_{ik} = \mathsf{E}_{ij}(\theta + \Delta\theta, \phi + \Delta\phi, \psi + \Delta\psi)\; \mathsf{E}_{kj}(\theta, \phi, \psi)$, we obtain,

$$\mathbf{G} = \begin{pmatrix} 1 & \Delta\phi\, c\theta + \Delta\psi & -\Delta\theta\, c\psi - \Delta\phi\, s\theta\, s\psi \\ -\Delta\phi\, c\theta - \Delta\psi & 1 & \Delta\theta\, s\psi - \Delta\phi\, s\theta\, c\psi \\ \Delta\theta\, c\psi + \Delta\phi\, s\theta\, s\psi & -\Delta\theta\, s\psi + \Delta\phi\, s\theta\, c\psi & 1 \end{pmatrix}. \tag{A.21}$$

One can thus obtain the rotation rates as,

$$\dot{\theta} = s\psi\, \widetilde{B}'_{23} + c\psi\, \widetilde{B}'_{31},$$

$$\dot{\phi} = -\frac{c\psi}{s\theta}\, \widetilde{B}'_{23} + \frac{s\psi}{s\theta}\, \widetilde{B}'_{31},$$

$$\dot{\psi} = \widetilde{B}'_{12} + \frac{c\theta\, c\psi}{s\theta}\, \widetilde{B}'_{23} - \frac{c\theta\, s\psi}{s\theta}\, \widetilde{B}'_{31}.$$

It is instructive to compare equations (A1-A6) with the corresponding equations in a plane for a material ellipse in an arbitrary strain field. The equations describing its principal axes and its orientation are,

$$\dot{a_1} = a_1\, \widetilde{A}'_{11}, \tag{A.22}$$

$$\dot{a_2} = a_2\, \widetilde{A}'_{22}, \tag{A.23}$$

$$\dot{\psi} = \widetilde{B}'_{12}, \tag{A.24}$$

where the primed system refers to the the principal axes of the ellipse and,

$$\mathsf{E} = \begin{pmatrix} \cos\psi & \sin\psi \\ -\sin\psi & \cos\psi \end{pmatrix}.$$

Equations A.22 – A.24 when written in the lab frame are (Kida 1981),

$$\dot{a_1} = a_1\, \lambda\, \cos 2\psi,$$

$$\dot{a_2} = -\, a_2\, \lambda\, \cos 2\psi,$$

$$\dot{\psi} = \Omega + \lambda\, \frac{a_2^2 + a_1^2}{a_2^2 - a_1^2}\, \sin 2\psi,$$

where,

$$\mathbf{S} = \begin{pmatrix} \lambda & -\Omega \\ \Omega & -\lambda \end{pmatrix}.$$

This system has a Hamiltonian structure (Neu 1984) and can be written in a compact form. Define two scaled variables η and τ as,

$$\eta = a_1/a_2, \tag{A.25}$$

$$\frac{d\tau}{dt} = \Omega \frac{\eta^2}{\eta^2 - 1}. \tag{A.26}$$

With this transformation the equations are,

$$\begin{aligned} \dot{\eta} &= \eta\,(2\lambda \cos 2\psi), \\ \dot{\psi} &= \Omega + \lambda \frac{1+\eta^2}{1-\eta^2} \sin 2\psi. \end{aligned}$$

Then we can write the Hamiltonian as,

$$H = \left(\eta + \frac{1}{\eta}\right) - \frac{\lambda}{\Omega}\left(\eta - \frac{1}{\eta}\right) \sin 2\psi, \tag{A.27}$$

with,

$$\eta_\tau = -\frac{\partial H}{\partial \psi}\ ;\ \psi_\tau = \frac{\partial H}{\partial \eta}. \tag{A.28}$$

Appendix B

Vortex in a linear background field

Consider a vortex embedded in a background linear velocity field, the latter viewed as generated by the velocity gradients of the local resolved flow. Denote laboratory-fixed axes by x_i and vortex-fixed axes by r_i; for clarity we omit the "prime" superscript on vortex-fixed quantities. Without loss of generality these two axis systems may be chosen to be coincident at time $t = 0$. The fluid velocity in the fixed frame is q_i and the vorticity is $\xi_i = \varepsilon_{ijk}\partial q_k/\partial x_j$, whilst in vortex-fixed axes these are v_i and $\zeta_i = \varepsilon_{ijk}\partial v_k/\partial r_j$ respectively, where ε_{ijk} used with a triple subscript here denotes the alternating tensor. The vortex rotates with angular velocity $\Omega_i(t)$ with respect to the x_i in a way to be described. The background field is

$$\tilde{q}_i = \tilde{A}_{ij}(t)\, x_j \equiv \tilde{S}_{ij}(t)\, x_j + \tilde{Q}_{ij}(t)\, x_j, \tag{B.1}$$

where $\tilde{S}_{ij}(t)$ is the symmetric and $\tilde{Q}_{ij}(t) = \frac{1}{2}\varepsilon_{ijk}\tilde{\xi}_k(t)$ the antisymmetric part of $\tilde{A}_{ij}(t)$, and $\tilde{\xi}_i(t)$ is the background vorticity. The time dependencies of all these quantities, which differ in laboratory and in vortex-fixed axes, will be suppressed unless required. In particular we note that the background strain tensor $\tilde{S}_{ij}(t)$ and vorticity $\tilde{\xi}_k(t)$ are not independent, since the latter subject to stretching and tilting by $\tilde{S}_{ij}(t)$. Let $u_i(\mathbf{r}, t)$ be the velocity field associated with the vortex alone, in vortex fixed axes, and ω_i the corresponding vorticity, $\omega_i = \varepsilon_{ijk}\partial u_k/\partial r_j$. The full velocity and vorticity in the vortex-fixed (rotating) axes are then

$$\zeta_i\,(\mathbf{r}, t) = \tilde{\xi}_i - 2\,\Omega_i + \omega_i, \tag{B.2}$$

$$v_i\,(\mathbf{r}, t) = \tilde{A}_{ij}\, r_j - \varepsilon_{ijk}\,\Omega_j\, r_k + u_i. \tag{B.3}$$

The components of v_i are

$$\begin{aligned} v_1 - u_1 &= \tilde{A}_{11}\, r_1 + (\tilde{A}_{12} + \Omega_3)\, r_2 + (\tilde{A}_{13} - \Omega_2)\, r_3, \\ v_2 - u_2 &= (\tilde{A}_{21} - \Omega_3)\, r_1 + \tilde{A}_{22}\, r_2 + (\tilde{A}_{23} + \Omega_1)\, r_3, \end{aligned} \tag{B.4}$$

$$v_3 - u_3 \;=\; (\tilde{A}_{31} + \Omega_2)\, r_1 + (\tilde{A}_{32} - \Omega_1)\, r_3 + \tilde{A}_{33}\, r_3.$$

In vortex-fixed axes, the momentum and vorticity equations may be written, respectively, as

$$\frac{\partial}{\partial t}\left(v_i + \varepsilon_{ijk}\,\Omega_j\, r_k\right) + v_j\,\frac{\partial v_i}{\partial r_j} + 2\,\varepsilon_{ijk}\,\Omega_j\, v_k \;=\; \frac{\partial P^*}{\partial r_j} + \nu\,\nabla^2_{r_i}\, v_i, \tag{B.5}$$

$$\frac{\partial}{\partial t}\left(\tilde{\zeta}_i + 2\,\tilde{\Omega}_i\right) + v_j\,\frac{\partial \tilde{\zeta}_i}{\partial r_j} \;=\; (\tilde{\zeta}_j + 2\,\Omega_j)\,\frac{\partial v_i}{\partial r_j} + \nu\,\nabla^2_{r_i}\zeta_i, \tag{B.6}$$

where $P^* = P + \frac{1}{2}\,\Omega^2\, r_i^2$ and P is the pressure. Continuity is $\partial v_i/\partial r_i = 0$.

At $t = 0$ we specify that $\omega_i = \omega_i(r_1, r_2, 0)$ (hence $u_i = u_i(r_1, r_2, 0)$) and $r^2\omega_i \to 0$ as $r_1^2 + r_2^2 \to \infty$. Thus there is initially no dependence on the r_3 coordinate, which is viewed as the 'axis' of the vortex, and the vorticity is compact in the cross-sectional plane, $(r_1 - r_2)$. It follows from (B4-B6) and the initial conditions that the absence of dependence on r_3, i.e., $\omega_i = \omega_i(r_1, r_2, t)$, $u_i = u_i(r_1, r_2, t)$, will be preserved in the evolution provided $\Omega_1 = -\tilde{A}_{23}$, $\Omega_2 = \tilde{A}_{13}$. The component Ω_3 is arbitrary and a convenient choice is $\Omega_3 = -\tilde{A}_{12}$. Introduction of a vector potential $\Psi_i(r_1, r_2, t)$ such that

$$u_i = \varepsilon_{ijk}\,\frac{\partial \Psi_k}{\partial r_j}, \qquad \frac{\partial \Psi_i}{\partial r_i} = 0, \quad \omega_i = -\nabla^2_{r_i}\,\Psi_i, \tag{B.7}$$

then allows (B4) to be written in the form

$$\begin{aligned} v_1 &= \tilde{S}_{11}\, r_1 + \frac{\partial \Psi_3}{\partial r_2}, \\ v_2 &= 2\tilde{S}_{12}\, r_1 + \tilde{S}_{22}\, r_2 - \frac{\partial \Psi_3}{\partial r_1}, \\ v_3 &= 2\tilde{S}_{13}\, r_1 + 2\tilde{S}_{23}\, r_2 + \tilde{S}_{33}\, r_3 + \frac{\partial \Psi_2}{\partial r_1} - \frac{\partial \Psi_1}{\partial r_2}. \end{aligned} \tag{B.8}$$

When (B8) and (B2) are used in (B6), the resulting equations together with the third of (B7) give closed equations for $\omega_i(r_1, r_2, t)$. Similarly, closed equations for $u_i(r_1, r_2, t)$ may be obtained from (B5).

It is straightforward that the above choice for Ω_i is equivalent to rotation of the r_3 axis according to

$$\frac{\partial e_i}{\partial t} = e_j\,\tilde{A}_{i,j} - e_i\, e_k\, e_j\,\tilde{A}_{k,j}, \tag{B.9}$$

where $e_i(t) \equiv e_i^v$ (text usage) are the direction cosines of the r_3 axis relative to the laboratory axes, $(\mathbf{e}(0) = (0,0,1))$. This is just the rotation that would be experienced by a material line element of unit length aligned with the vortex axis, due to the linear field alone; it provides a derivation of equation (2.21). The vortex axis remains rectilinear and the internal structure of the vortex is two-dimensional in the sense of dependence only on (r_1, r_2), but allows axial flow.

To obtain the enstrophy equation we simplify to the special case where there is no background vorticity $\xi_i = 0$. This may be a reasonable model for a strong vortex $|\omega_i| >> |\tilde{\xi}_i|$. We also put $\omega_1 = \omega_2 = 0$ at $t = 0$, from which it follows from the vorticity equation, that this will be true for all $t > 0$. The ω_3 vorticity equation is then

$$\frac{\partial \omega_3}{\partial t} + \left(\tilde{S}_{11}\, r_1 + \frac{\partial \Psi_3}{\partial r_2}\right) \frac{\partial \omega_3}{\partial r_1} + \left(2\tilde{S}_{12}\, r_1 + \tilde{S}_{22}\, r_2 - \frac{\partial \Psi_3}{\partial r_1}\right) \frac{\partial \omega_3}{\partial r_1} = \tilde{S}_{33}\, \omega_3 + \nu\, \nabla^2_{r_i} \omega_3. \quad \text{(B.10)}$$

Now multiply (B10) by ω_3, integrate over the $(r_1 - r_2)$ plane and use the well-known results, valid for the vortex flow, $\nu\, \overline{\omega_3\, \nabla^2_{r_i} \omega_3} = 2\nu \int_0^\infty k^4\, E(k)\, dk$ and $\epsilon_{sgs} = \nu\, \overline{\omega_3^2}$, where $E(k)$ is the shell-summed energy spectrum and where the overbar refers to an integral over the vortex cross-section. This gives, after some algebra

$$\frac{\partial \overline{\epsilon}_{sgs}}{\partial t} = \tilde{S}_{33}\, \overline{\epsilon}_{sgs} - 4\nu^2 \int_0^\infty k^4\, E(k)\, dk. \quad \text{(B.11)}$$

Finally, we account for the stretching or compression of the vortex by $\tilde{S}_{33}$ and for an average over all possible spin angles of the vortex structure about the r_3 axis. Denoting the vortex length at time by $l(t)$ we write for some quantity f

$$\overline{\overline{f}} = \frac{l(t)}{2\,\pi L^3} \int_{-\infty}^{\infty} \int_{-\infty}^{\infty} \int_0^{2\pi} f\, dr_1\, dr_2\, d\gamma, \qquad l\,(t) = l\,(0) \exp\left(\int_0^t \tilde{S}_{33}(t')\, dt'\right), \quad \text{(B.12)}$$

where the double overbar denotes integration over r_3 (equivalent to multiplying by $l\,(t)$) and the vortex cross section, division by the volume L^3 of a large box containing a vortex and an average over all possible spin angles γ, $0 \le \gamma \le 2\pi$. Differentiating the first of (B12) with respect to t and using the second of (B12) then gives

$$\frac{\partial \overline{\overline{f}}}{\partial t} = \tilde{S}_{33}\, \overline{\overline{f}} + \frac{\partial}{\partial t}\left(\frac{l\,(t)}{2\,\pi L^3} \int_{-\infty}^{\infty} \int_{-\infty}^{\infty} \int_0^{2\pi} f\, dr_1\, dr_2\, d\gamma\right). \quad \text{(B.13)}$$

When the first of (B12) is applied to (B11) ($f \equiv \epsilon_{sgs}$) and (B13) is used for the unsteady term it is found that

$$\frac{\partial \overline{\overline{\epsilon}}_{sgs}}{\partial t} = 2\,\tilde{S}_{33}\,\overline{\overline{\epsilon}}_{sgs} - 4\nu^2 \int_0^\infty k^4\,E(k)\,dk, \tag{B.14}$$

and we note that the double overbar has been suppressed for $E(k)$. Omitting the double overbar on the other terms gives equation(5.2).

An energy equation for the internal vortex motions may be obtained along similar lines, starting with (B5). Care must be taken to account for the contribution from the pressure at infinity in the $r_1 - r_2$-plane and the time variation of $\tilde{S}_{ij}(t)$ in the vortex-fixed frame. Defining $K = \frac{1}{2}\left(\overline{\overline{u_1^2}} + \overline{\overline{u_2^2}}\right)$ and invoking equipartition $\overline{\overline{u_1^2}} = \overline{\overline{u_2^2}}$, $\overline{\overline{u_1\,u_2}} = 0$ in vortex-fixed axes following averaging over spin angle, and using

$$\frac{l\,(t)}{2\,\pi L^3} \int_0^{2\pi} \nu \left(\overline{\overline{u_1\,\nabla^2_{r_i}\,u_1 + u_2\,\nabla^2_{r_i}\,u_2}}\right) d\gamma = -2\nu \int_0^\infty k^2\,E(k)\,dk, \tag{B.15}$$

one obtains, after some algebra

$$\frac{\partial K}{\partial t} = \tilde{S}_{33}\,K - 2\nu \int_0^\infty k^2\,E(k)\,dk. \tag{B.16}$$

Appendix C

Initialization of the velocity field in homogeneous turbulence

The Fourier coefficients are evaluated given the energy spectrum. We make the following choice for the Fourier coefficient satisfying the divergence free constraint.

$$\widehat{\widetilde{U}} = \begin{cases} \dfrac{\alpha k k_2 + \beta k_1 k_3}{k(k_1^2+k_2^2)^{1/2}}\mathbf{e_1} + \dfrac{\beta k_2 k_3 - \alpha k k_1}{k(k_1^2+k_2^2)^{1/2}}\mathbf{e_2} - \dfrac{\beta(k_1^2+k_2^2)^{1/2}}{k}\mathbf{e_3} & \text{if } k_1 \& k_2 \neq 0, \\ \alpha\mathbf{e_1} + \beta\mathbf{e_2} + 0\mathbf{e_3} & \text{otherwise,} \end{cases} \tag{C.1}$$

where,

$$\alpha(k) = \left(\frac{E(k)}{2\pi k^2}\right)^{1/2} e^{i\theta_1}\cos\phi, \tag{C.2}$$

$$\beta(k) = \left(\frac{E(k)}{2\pi k^2}\right)^{1/2} e^{i\theta_1}\sin\phi, \tag{C.3}$$

if $k \neq 0$ and $\alpha = \beta = 0$ if $k = 0$. $E(k)$ is the shell-summed energy spectrum and θ_1, θ_2 and ϕ are random numbers uniformly distributed in the interval $(0, 2\pi)$. See Huang (1994) for details.

Appendix D

Two-dimensional energy spectrum

We wish to derive the two-dimensional energy spectrum for the stretched vortex models. We first consider general relationships for homogeneous turbulence.

We define the two-dimensional spectrum tensor as,

$$\Theta_{ij}(k_1,k_2) = \frac{1}{2\pi}\int_{-\infty}^{\infty}\int_{-\infty}^{\infty} R_{ij}(\rho_1,\rho_2,0)e^{-ik_1\rho_1 - ik_2\rho_2}d\rho_1 d\rho_2, \tag{D.1}$$

where the two-point velocity correlation tensor is given by,

$$R_{ij}(\rho) = \int_{-\infty}^{\infty}\int_{-\infty}^{\infty}\int_{-\infty}^{\infty}\phi_{ij}(\mathbf{k}')e^{-i\mathbf{k}'\cdot\rho}dk_1'dk_2'dk_3'. \tag{D.2}$$

Therefore,

$$R_{ij}(\rho_1,\rho_2,0) = \int_{-\infty}^{\infty}\int_{-\infty}^{\infty}\int_{-\infty}^{\infty}\phi_{ij}(\mathbf{k}')e^{-ik_1'\rho_1 - ik_2'\rho_2}dk_1'dk_2'dk_3'. \tag{D.3}$$

Substituting (D.3) in (D.1), we obtain,

$$\Theta_{ij}(k_1,k_2) = \int_{-\infty}^{\infty}\phi_{ij}(k_1,k_2,k_3)dk_3. \tag{D.4}$$

We define a two-dimensional energy spectrum tensor as

$$\Psi_{ij}(\mathrm{K}) = \mathrm{K}\int_0^{2\pi}\Theta_{ij}d\chi, \tag{D.5}$$

where

$$k_1 = \mathrm{K}\cos\chi, \tag{D.6}$$

$$k_2 = \mathrm{K}\sin\chi. \tag{D.7}$$

K is the two-dimensional wavenumber such that $\mathrm{K}^2 = k_1^2 + k_2^2$ and $\mathrm{K}^2 + k_3^2 = k^2$.

The above relationships are general. We now specialize to the stretched-vortex models

developed in Chapter 2. PS give an extensive derivation of the one-dimensional spectra for such models. Here, we adapt their analysis to obtain the two-dimensional spectrum for the stretched-vortex model. This is required in the implementation of the channel flow. We begin by replacing PS-(40) by the two-dimensional spectrum tensor,

$$\Theta_{ij}(k_1,k_2) = \frac{1}{16\pi^3 L^3}\sum \ell_m \int\int\ldots\int\int \tag{D.8}$$
$$|\omega|^2\frac{1}{k^2}\left(\delta_{ij}-\frac{k_ik_j}{k^2}-\mathsf{E}_{3i}\mathsf{E}_{3j}\right)e^{-i(k_q+\mathsf{E}_{1q}\kappa_1+\mathsf{E}_{2q}\kappa_2)\rho_q}P(\alpha,\beta,\gamma)dk_3d\rho_1d\rho_2d\rho_3d\kappa_1d\kappa_2d\Omega$$

where $d\Omega = \sin\alpha d\alpha d\beta d\gamma$. We now follow steps after PS-(40) and perform the following operations:

(i) Integrate w.r.t ρ_1,ρ_2,ρ_3. Use PS-(41) for the δ functions.

(ii) Perform k_3 integration and use $k_3+\mathsf{E}_{i3}\kappa_1+\mathsf{E}_{23}\kappa_2=0$ (PS-(43)).

(iii) Substitute (D.8) $\rightarrow$ (D.5), to obtain

$$\Psi_{ij}(\mathrm{K}) = \frac{\mathrm{K}}{2L^3}\sum \ell_m \int\int\ldots\int\int \tag{D.9}$$
$$|\omega|^2\frac{1}{k^2}\left(\delta_{ij}-\frac{k_ik_j}{k^2}-\mathsf{E}_{3i}\mathsf{E}_{3j}\right)\delta(k_1+\mathsf{E}_{11}\kappa_1+\mathsf{E}_{21}\kappa_2)\delta(k_2+\mathsf{E}_{12}\kappa_1+\mathsf{E}_{22}\kappa_2)$$
$$P(\alpha,\beta,\gamma)d\kappa_1d\kappa_2d\chi\sin\alpha d\alpha d\beta d\gamma.$$

Next we perform integration w.r.t. γ and χ.

(i) Assume $P(\alpha,\beta,\gamma)$ is independent of γ.

(ii) Use

$$\delta[f(\gamma,\chi)]\delta[g(\gamma,\chi)] = \sum_{q=1}^{Q}\frac{\delta(\gamma-\gamma_q)\delta(\chi-\chi_q)}{J(\gamma_q,\chi_q)}, \tag{D.10}$$

where,

$$f(\gamma,\chi) = k_1+\mathsf{E}_{11}\kappa_1+\mathsf{E}_{21}\kappa_2, \tag{D.11}$$
$$g(\gamma,\chi) = k_2+\mathsf{E}_{12}\kappa_1+\mathsf{E}_{22}\kappa_2, \tag{D.12}$$
$$J(\gamma_q,\chi_q) = \begin{vmatrix} \frac{\partial f}{\partial\chi} & \frac{\partial g}{\partial\chi} \\ \frac{\partial f}{\partial\gamma} & \frac{\partial g}{\partial\gamma} \end{vmatrix} \tag{D.13}$$

$f(\gamma_q,\chi_q)=g(\gamma_q,\chi_q)=0, q=1\ldots Q.$

(iii) Put $\kappa_1 = \kappa\cos\theta_k$, $\kappa_2 = \kappa\sin\theta_k$; $d\kappa_1 d\kappa_2 = \kappa d\kappa d\theta_k$.

(iv) Use

$$\int_0^{2\pi}\int_0^{\infty}\int_0^{2\pi}\int_0^{\pi} F(\kappa,\theta_k;\gamma,\chi) \tag{D.14}$$
$$\delta(k_1+\mathsf{E}_{11}\kappa_1+\mathsf{E}_{21}\kappa_2)\delta(k_2+\mathsf{E}_{12}\kappa_1+\mathsf{E}_{22}\kappa_2)\kappa d\kappa d\theta_k d\chi d\gamma$$
$$=\sum_{q=0}^{Q}\int_0^{2\pi}\int_{\kappa}\frac{F(\kappa,\theta_k|\gamma,\chi)d\kappa d\theta_k}{J(\gamma_q,\chi_q)}$$

where the sum is over all roots of (D.11) and (D.12).

After some algebra, using (D.11-D.13) and $k^2=\kappa^2$, it can be shown that

$$J=(\kappa^2-\mathrm{K}^2)^{1/2}(\mathrm{K}^2-\kappa^2\cos^2\alpha)^{1/2}. \tag{D.15}$$

This fixes the range of integration of κ. We therefore arrive at,

$$\Psi_{ij}(\mathrm{K})=\frac{\mathrm{K}}{2L^3}\sum\ell_m\int_0^{2\pi}\int_0^{\pi}\int_0^{2\pi}\int_{\mathrm{K}}^{|\frac{\mathrm{K}}{\cos\alpha}|} \tag{D.16}$$
$$|\omega|^2\times\frac{1}{k^2}\left(\delta_{ij}-\frac{k_ik_j}{k^2}-\mathsf{E}_{3i}\mathsf{E}_{3j}\right)\frac{\hat{P}(\alpha,\beta)\sin\alpha\,d\alpha\,d\beta\,d\kappa\,d\theta_k\,\kappa}{(\kappa^2-\mathrm{K}^2)^{1/2}(\mathrm{K}^2-\kappa^2\cos^2\alpha)^{1/2}}.$$

Let us now consider a two-dimensional (circle summed) energy spectrum

$$E_{2D}(\mathrm{K})=\frac{1}{2}\Psi_{ii};\ \delta_{ii}-\frac{k_ik_i}{k^2}-\mathsf{E}_{3i}\mathsf{E}_{3i}=1. \tag{D.17}$$

Using (D.16), and noting that the full shell-summed energy spectrum for the stretched-vortex model can be written as (PS-(48))

$$E(\kappa)=\frac{2\pi}{L^3}\sum_m\ell_m\int_0^{2\pi}\frac{1}{\kappa}|\omega|^2d\theta_k, \tag{D.18}$$

the 2D energy spectrum then becomes

$$E_{2D}(\mathrm{K})=\frac{\mathrm{K}}{2\pi^2}\int_0^{\pi}\int_0^{2\pi}\int_{\mathrm{K}}^{|\frac{\mathrm{K}}{\cos\alpha}|}\frac{E(\kappa)\hat{P}(\alpha,\beta)\sin\alpha d\alpha d\beta d\kappa}{(\kappa^2-\mathrm{K}^2)^{1/2}(\mathrm{K}^2-\kappa^2\cos^2\alpha)^{1/2}}. \tag{D.19}$$

We check this formula by putting $\hat{P}=1$ for isotropic turbulence. We find that the energy spectrum is given by, $E_{2D}(\mathrm{K})=\mathrm{K}\int_{\mathrm{K}}^{\infty}\frac{E(\kappa)d\kappa}{\kappa(\kappa^2-\mathrm{K}^2)}$. This has been verified independently to be

correct. We now make a choice for the shell-summed energy spectrum as

$$E(\kappa) = \mathcal{K}_0 \epsilon^{2/3} \kappa^{-5/3}, \tag{D.20}$$

where, C_κ is the Kolmogorov constant. Furthermore making a choice for $\hat{P}(\alpha, \beta)$ as that given by (2.12), we then obtain,

$$E_{2D}(\mathrm{K}) = \frac{2\mathcal{K}_0 \epsilon^{2/3} \mathrm{K}^{-5/3}}{\pi} \int_1^{\left|\frac{1}{\cos\alpha_0}\right|} \frac{u^{-5/3} du}{(u^2-1)^{1/2}(1-u^2\cos^2\alpha)^{1/2}} \tag{D.21}$$

$$= Q(\alpha_0)\mathcal{K}_0 \epsilon^{2/3} \mathrm{K}^{-5/3}. \tag{D.22}$$

Thus,

$$Q(\alpha_0) = \frac{2}{\pi} \int_1^{\left|\frac{1}{\cos\alpha_0}\right|} \frac{u^{-5/3} du}{(u^2-1)^{1/2}(1-u^2\cos^2\alpha)^{1/2}}. \tag{D.23}$$

We note that $Q(\alpha_0) = Q(\pi - \alpha_0)$. A plot of $Q(\alpha_0)$ is shown in Figure D.1 and in the numerical implementation of the model we evaluate it using a look-up table.

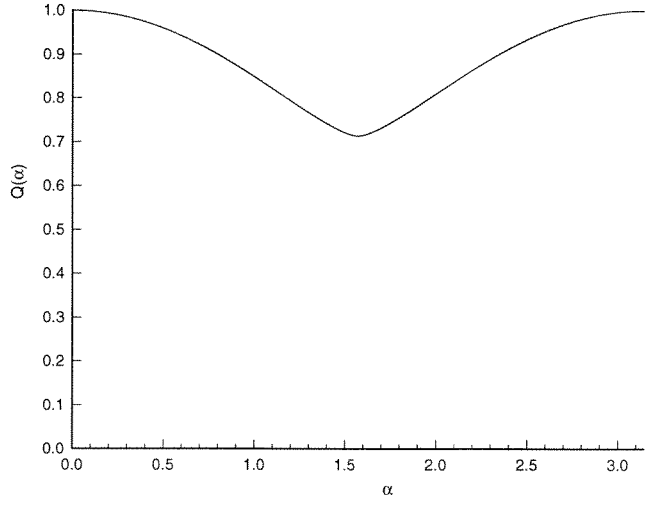

Figure D.1: $Q(\alpha)$ versus α.